

Baryogenesis and gravity waves from a UV-completed electroweak phase transition

Benoit Laurent* and James M. Cline†

McGill University, Department of Physics, 3600 University St., Montréal, QC H3A2T8 Canada

Avi Friedlander‡

Queen's University, Department of Physics & Engineering Physics
Astronomy Kingston, Ontario, K7L 3N6 Kingston, Canada

Dong-Ming He§

University of Science and Technology of China, Hefei, Anhui 230026 and
Universiteit van Amsterdam, Science Park 904, Amsterdam, 1098XH, Netherlands

Kimmo Kainulainen¶

Department of Physics, P.O.Box 35 (YFL), FIN-40014 University of Jyväskylä, Finland and
Helsinki Institute of Physics, P.O. Box 64, FIN-00014 University of Helsinki, Finland

David Tucker-Smith**

Department of Physics, Williams College, Williamstown, MA 01267

We study gravity wave production and baryogenesis at the electroweak phase transition, in a real singlet scalar extension of the Standard Model, including vector-like top partners to generate the CP violation needed for baryogenesis. The singlet makes the phase transition strongly first-order through its coupling to the Higgs boson, and it spontaneously breaks CP invariance through a dimension-5 contribution to the top quark mass term, generated by integrating out the heavy top quark partners. We improve on previous studies by incorporating updated transport equations, compatible with large bubble wall velocities v_w , to determine the friction on the wall, and thereby v_w and the wall thickness, rather than treating these as free parameters. The baryon asymmetry is also computed with no assumptions, directly from the microphysical parameters. The size of the CP-violating dimension-5 operator is constrained by collider, electroweak precision, and renormalization group running constraints. We identify regions of parameter space that can produce the observed baryon asymmetry, and simultaneously produce gravitational waves that could be observed by future experiments. Contrary to standard lore, we find that for strong deflagrations, the efficiencies of large baryon asymmetry production and strong GW-signal can be *positively* correlated.

CONTENTS

I. Introduction	2
II. Z_2 -symmetric singlet model	3
A. Laboratory constraints	4
B. Explicit breaking of Z_2 symmetry	6
III. Phase Transition and Bubble Nucleation	7
IV. Wall velocity and shape	8
A. Transport equations for fluid perturbations	10
V. Cosmological signatures	11
A. Gravitational Waves	11
B. Baryogenesis	12

* benoit.laurent@mail.mcgill.ca

† jcline@physics.mcgill.ca

‡ avi.friedlander@queensu.ca

§ dong-ming.he@student.uva.nl

¶ kimmo.kainulainen@jyu.fi

** dtuckers@williams.edu

VI. Monte Carlo results	13
A. Deflagration versus detonation solutions	14
B. Baryogenesis and gravity wave production	15
C. Dependence on λ_s and Λ	17
D. Theoretical uncertainties	17
E. Comparison of the GW signal with previous studies	19
VII. Conclusion	20
A. Effective Potential	20
B. Relativistic fluid equation	22
C. Gravitational Wave Production	23
References	24

I. INTRODUCTION

Phase transitions in the early universe provide an opportunity for probing physics at high scales through cosmological observables, in particular, if the transition is first order. In that case, it may be possible to explain the origin of baryonic matter through electroweak baryogenesis (EWBG) [1–4] or variants thereof [5]. Such transitions can also produce relic gravitational waves (GWs) that may be detectable by future experiments like LISA [6, 7], BBO [8], DECIGO [9, 10] and AEDGE [11].

It is remarkable that even though the electroweak phase transition (EWPT) is a smooth crossover in the standard model (SM) [12, 13], it can become first order with the addition of modest new physics input, in particular a singlet scalar coupling to the Higgs [14–20], that can also be probed in collider experiments [21–29]. There have been many studies of such new physics models with respect to their potential to produce observable cosmological signals [30–42]. However, it is challenging to make a first-principles connection between microphysical models and the baryon asymmetry or GW production, since these can be sensitive to the velocity v_w and thickness L_w of the bubble walls in the phase transition, which are numerically demanding to compute [43–53]. Most previous studies that encompass EWBG and GW studies of the EWPT therefore leave v_w and L_w as free parameters. This limitation was addressed recently in Ref. [54], which undertook a comprehensive investigation of the EWPT enhanced by coupling the Higgs boson to a scalar singlet with Z_2 symmetry. The simplicity of this model facilitates doing an exhaustive search of its parameter space.

In the present work we continue the investigation started in Ref. [54], which determined v_w and L_w over much of the model parameter space, but did not try to predict the baryon asymmetry or GW production. Moreover, that study was limited to subsonic wall speeds, due to a breakdown of the fluid equations that determine the friction on the wall. Recently a set of improved fluid equations was postulated in Refs. [55, 56], that do not suffer from the subsonic limitation. We use these in the present work in order to fully explore the parameter space, where high v_w can be favorable to observable GWs, and also compatible with EWBG. It will be shown that for strong deflagrations, the fluid velocity in front of the wall saturates and even decreases with increasing wall velocity v_w . Since the walls become thinner at the same time, the baryon asymmetry is enhanced at larger wall velocities for these transitions, becoming *positively* correlated with a strong GW signal.

A further improvement in this work is to present an ultraviolet completion of the effective coupling that gives rise to the CP-violation needed for EWBG. We introduce heavy vectorlike top partners which when integrated out induce a CP-violating coupling of the singlet scalar s to top quarks, giving the source term for EWBG.¹ We present the details in section II, including comprehensive laboratory constraints on the top partners and the subsequent constraints on the effective theory. The finite-temperature effective potential of the theory is also outlined there.

¹ Hints of the presence of such a particle in LHC data were recently presented in Ref. [57]

The paper continues in Sect. III with a brief description of our methodology for finding the high-temperature first-order phase transitions, and characterizing their strength. This is followed in Sect. IV by a detailed account of how the bubble wall speed and shape are determined. The techniques for computing the baryon asymmetry and GW production are described in Sect. V. We present the results of a Monte Carlo exploration of the model parameter space with respect to these observables in Sect. VI, with emphasis on the overlap between successful EWBG and potentially observable GWs. Conclusions are given in Sect. VII, followed by several appendices containing details about construction of the finite-temperature effective potential, solving junction conditions for the phase transition boundaries, and predicting GW production.

II. Z_2 -SYMMETRIC SINGLET MODEL

We study the Z_2 -symmetric singlet scalar extension of the SM with a real singlet s coupled to the Higgs doublet H . The scalar potential is

$$V(H, s) = \mu_h^2 H^\dagger H + \lambda_h (H^\dagger H)^2 + \frac{\lambda_{hs}}{2} (H^\dagger H) s^2 + \frac{\mu_s^2}{2} s^2 + \frac{\lambda_s}{4} s^4. \quad (1)$$

We work in unitary gauge, which consists of taking $H = h/\sqrt{2}$; the Goldstone bosons still contribute to the one-loop and thermal corrections, but they are set to zero in the tree-level potential. We assume $\mu_h^2 < 0$ and $\mu_s^2 < 0$, which implies that the potential has non-trivial minimums at $v \equiv h = \pm|\mu_h|/\sqrt{\lambda_h} \approx 246$ GeV, $s = 0$ and $h = 0$, $s = \pm|\mu_s|/\sqrt{\lambda_s}$. The scalar fields' mass in the vacuum can then be written in terms of the parameters of the potential as $m_h^2 = -2\mu_h^2 \approx (125 \text{ GeV})^2$ and $m_s^2 = -\lambda_{hs}\mu_h^2/(2\lambda_h) + \mu_s^2$.

The other relevant interaction of s is a dimension-5 operator yielding an imaginary contribution to the top quark mass [58]:

$$\mathcal{L}_{BG} = -\frac{y_t}{\sqrt{2}} h \bar{t}_L \left(1 + i \frac{s}{\Lambda} \right) t_R + \text{H.c.} \quad (2)$$

This term will be ignored during the discussion on the phase transition; however it is essential for generating the baryon asymmetry, since it gives the CP-violating source term when s temporarily gets a VEV in the bubble walls of the electroweak phase transition. In Eq. (2) we have adopted a special limit of a more general model, in which the dimension-5 contribution is purely imaginary. This can be understood as a consequence of imposing CP in the effective Lagrangian, with s coupling like a pseudoscalar, $s \rightarrow -s$. Hence it is consistent to omit terms odd in s in the scalar potential (1), even though Eq. (2) is odd in s . The CP symmetry prevents a VEV from being generated for s by loops.

The effective operator is generated by integrating out a heavy singlet vectorlike top quark partner T , whose mass term and couplings to the third generation quarks $q_L = (t_L, b_L)$, Higgs and singlet fields are

$$y_t \bar{q}_L H t_R + \eta_1 \bar{q}_L H T_R + i\eta_2 \bar{T}_L s t_R + M \bar{T}_L T_R + \text{H.c.} \quad (3)$$

including also the SM q_L -Higgs coupling. This is invariant under CP if $s \rightarrow -s$ ². Integrating out T leads to the effective operator in (2) with scale

$$\Lambda = \frac{y_t M}{\eta_1 \eta_2} \quad (4)$$

We consider experimental constraints on the scale Λ below.

In previous literature, thermal corrections were frequently approximated by including just the first term of the high-temperature expansion of the thermal functions presented in the Appendix B. However, this approximation fails at temperatures below the mass of particles strongly coupled to the Higgs, as can happen in models with a high degree of supercooling. Therefore, we employ the full one-loop thermal functions. This will be shown to have a large impact on the values of the tunneling action, and thus of the nucleation temperature. In addition to the tree-level potential and the thermal corrections, we also include the one-loop correction and the thermal mass Parwani resummation [59]. The complete effective potential then becomes

$$V_{\text{eff}} = V_{\text{tree}} + V_{\text{CW}} + V_T + \delta V. \quad (5)$$

The details are presented in Appendix A.

² The interaction term $i\eta_3 \bar{T}_L s T_R$ also respects CP for real η_3 . We neglect it to simplify our analysis.

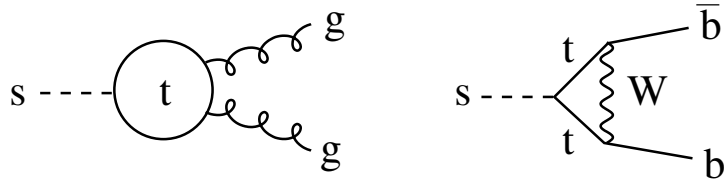


FIG. 1. Feynman diagrams for decay of the singlet s .

A. Laboratory constraints

It is important to determine how low the scale Λ of the dimension-5 operator in Eq. (4) can be, since it has a strong impact on the baryon asymmetry η_b ; in the limit of large Λ , η_b scales as $1/\Lambda$. The relevant masses and couplings are constrained by direct searches for the top partner and precision electroweak studies. Moreover the properties of the singlet s are constrained by collider searches.

After electroweak symmetry breaking, a Dirac mass term $(\bar{t}_L, \bar{T}_L)(\begin{smallmatrix} m_t & \mu \\ 0 & M \end{smallmatrix})(\begin{smallmatrix} t_R \\ T_R \end{smallmatrix})$ is generated for t, T , with $m_t = y_t v/\sqrt{2}$ and $\mu = \eta_1 v/\sqrt{2}$ that is diagonalized by separate rotations on (t_R, T_R) and (t_L, T_L) , with mixing angles

$$\tan 2\theta_L = 2 \frac{M\mu}{M^2 - m_t^2 - \mu^2}, \quad \tan 2\theta_R = 2 \frac{m_t\mu}{M^2 + \mu^2 - m_t^2}. \quad (6)$$

For example, consider a benchmark point with $\eta_1 = 0.55$ and a physical T mass $M_T = 800$ GeV. These parameters correspond to $M = 794$ GeV and mixing angles $\theta_L = 0.126$ and $\theta_R = 0.027$. The relation between y_t and the physical top mass differs from the SM one by less than 1%, which is allowed by current LHC constraints [60, 61]. For sufficiently large η_2 , decays of T to $ht/Zt/Wb$ induced by mixing are highly subdominant to $T \rightarrow st$, and searches for vector-like top partners that focus on the former channels are evaded. Near the Goldstone-equivalent limit (which should apply reasonably well for $M_T = 800$ GeV and relatively small s masses, $m_s \sim 100$ GeV), the branching ratio of $T \rightarrow st$ is

$$B(T \rightarrow st) \simeq \frac{\eta_2^2}{\eta_2^2 + 2\eta_1^2}. \quad (7)$$

We roughly estimate from Refs. [62, 63] that for $M_T = 800$ GeV, vector-like quark searches that target SM final states are evaded provided $B(T \rightarrow st) \gtrsim 90\%$, corresponding to $\eta \gtrsim 2.4$ for our benchmark point. Ref. [64] (see Fig. 1 of contribution 5; also [65]) has reinterpreted collider bounds to constrain the parameter space (m_s, M_T) for models in which $T \rightarrow st$ dominates, finding that top partner masses above ~ 750 GeV are allowed in the case where s decays 100% into two gluons. This is true in our model, where the dominant s decays are induced by the loop diagrams shown in Fig. 1. One can estimate that the gluon final state dominates over that of b quarks by a factor of $(g_s^2 m_s / g_w^2 m_b)^2 \gtrsim 10^3$, and over decays into photons by $(g_s/e)^4 \sim 300$. Precision electroweak data constrain the additional contributions to the oblique parameters, especially T , which is corrected by [66]

$$\Delta T = T_{\text{sm}} s_L^2 \left(-(1 + c_L^2) + s_L^2 r + 2c_L^2 \frac{r}{r-1} \ln r \right) \lesssim 0.1, \quad (8)$$

where $T_{\text{sm}} = 1.19$ is the SM value, $c_L = \cos \theta_L$, $s_L = \sin \theta_L$, and $r = (M_T/m_t)^2$; the upper limit is from section 10 of [67]. The benchmark point chosen above almost saturates this constraint, giving $\Delta T \simeq 0.09$.

There are also direct searches for resonant production of the singlet, by gluon-gluon fusion. The coupling of s to t in the mass eigenstate basis is $y_{st} = \eta_2 \cos \theta_R \sin \theta_L \sim \eta_2 \theta_L$, while that to T is $y_{sT} = -\eta_2 \cos \theta_L \sin \theta_R \sim -\eta_2 \theta_R$. The squared matrix element for the decays $s \rightarrow gg$ is [68]

$$|\mathcal{M}|^2 = \left(\frac{\alpha_s}{\pi} \right)^2 m_s^4 \left| \sum_{i=t,T} \frac{y_{si}}{m_i} \tau_i \left[\sin^{-1} \left(\tau_i^{-1/2} \right) \right]^2 \right|^2, \quad (9)$$

where $\tau_i = 4m_i^2/m_s^2$. The parton-level production cross section for $gg \rightarrow s$ is $\hat{\sigma} = \pi |\mathcal{M}|^2 \delta(\hat{s} - m_s^2)/(256 \hat{s})$, where the 256 comes from averaging over gluon colors and spins. Integrating this over the gluon PDFs gives the

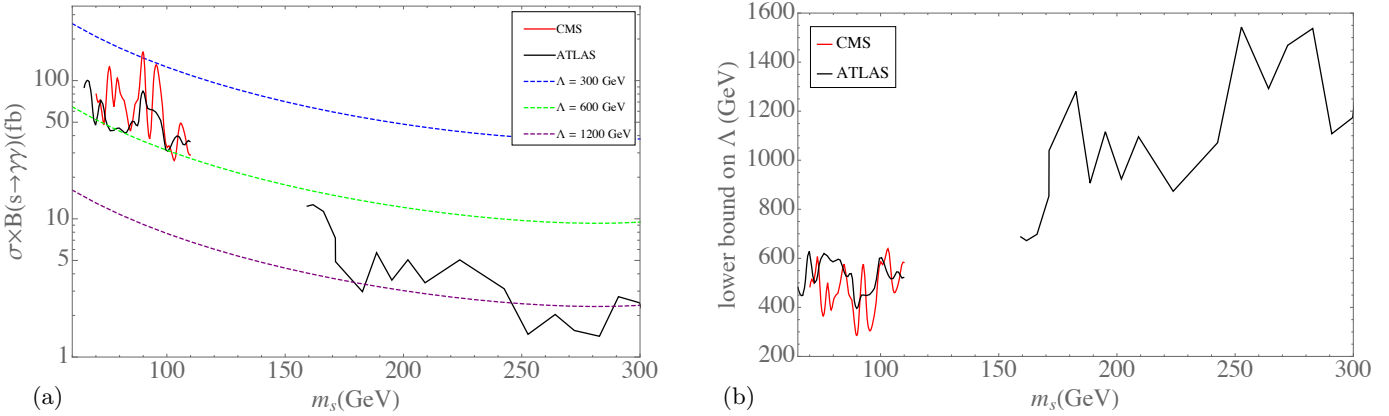


FIG. 2. Left (a): experimental limits from ATLAS [69, 70] and CMS [71] for resonant production of s by gg fusion followed by decays into photons (solid lines), versus predictions at different values of Λ . Right (b): corresponding lower bounds on Λ .

hadron-level cross section

$$\sigma(pp \rightarrow s) = \frac{\pi}{256 m_s^4} |\mathcal{M}|^2 \mathcal{L}_g \equiv \frac{\pi}{256 m_s^4} |\mathcal{M}|^2 \int_{m_s^2/s}^1 \frac{dx}{x} [xf_g](x) [xf_g](m_s^2/sx) \quad (10)$$

in which dependence on m_s drops out except in the parton luminosity factor \mathcal{L}_g . This production is probed via decays $s \rightarrow \gamma\gamma$, whose branching ratio is approximately $B(s \rightarrow \gamma\gamma) = (8/9)\alpha^2/\alpha_s^2$ [68]. For the dominant $s \rightarrow gg$ decay into gluons, in principle LHC dijet resonance searches could be constraining, but these exist only for $m_s \gtrsim 500$ GeV which is beyond the range of interest for the present study. To a good approximation, $\sigma(pp \rightarrow s)$ is determined by m_s and Λ . In Fig. 2(a) we show limits from ATLAS [69, 70] and CMS [71] on $\sigma B(s \rightarrow \gamma\gamma)$ as a function of m_s , along with the predictions for various Λ , and in Fig. 2(b) we show the associated lower bounds on Λ . In the low-mass region ($65 \text{ GeV} < m_s < 110 \text{ GeV}$), lower bounds on Λ range roughly from 400 GeV to 650 GeV; in the intermediate-mass region ($110 \text{ GeV} < m_s < 160 \text{ GeV}$), Λ is not bounded by diphoton resonance searches, and for much of the high-mass region ($m_s > 160$ GeV), Λ is bounded to be above 1 TeV. For our subsequent scans of parameter space, we adopt a fixed reference value for Λ ,

$$\Lambda_{\text{ref}} = 540 \text{ GeV}, \quad (11)$$

which is large enough to be consistent with much of the low- m_s region. Because Λ_{ref} is well below the lower-bounds on Λ in the high-mass region, we confine our scans to $m_s < 160$ GeV for consistency.³

We show the constraints from precision electroweak data, diphoton resonance searches, and vector-like quark searches in the η_1 - η_2 plane in Fig. 3, for $M_T = 800$ GeV, where we approximate the T search constraints by the requirement $B(T \rightarrow st) > 0.9$, and for $M_T = 1300$ GeV, heavy enough to evade T searches for any $B(T \rightarrow st)$. For the chosen m_s , it is apparent that the reference value $\Lambda = 540$ GeV is attainable for $\eta_2 \gtrsim 2.5$ for $M_T = 800$ GeV and $\eta_2 \gtrsim 3$ for $M_T = 1300$ GeV. For slightly heavier s in the window $110 \text{ GeV} < m_s < 160$ GeV, diphoton resonance searches are evaded and the red contours disappear. In this case even lower values of Λ are allowed provided one is willing to consider larger values of η_2 .

Because the baryon asymmetry η_b scales roughly as $1/\Lambda$, it is straightforward to reinterpret our final results for larger (or smaller) Λ . For example, from Fig. 5(c) one can infer that a significant fraction of points remain viable for baryogenesis for $\Lambda = 2\Lambda_{\text{ref}}$ (or for even larger Λ), a scale consistent with more modest couplings, $\eta_2 \sim 1.5$.

Allowing for very large values of η_2 could invalidate the effective theory above the heavy top partner threshold M at scales only slightly larger than M , which would require us to specify additional new physics in order to have

³ Although we do not pursue this point here, lower values of Λ are consistent with $m_s > 160$ GeV if $B(s \rightarrow \gamma\gamma)$ is suppressed due to, for example, a dominant invisible decay channel; LHC constraints on $t\bar{t}$ plus missing energy [72, 73] are in that case evaded for $M_T \gtrsim 1350$ GeV.

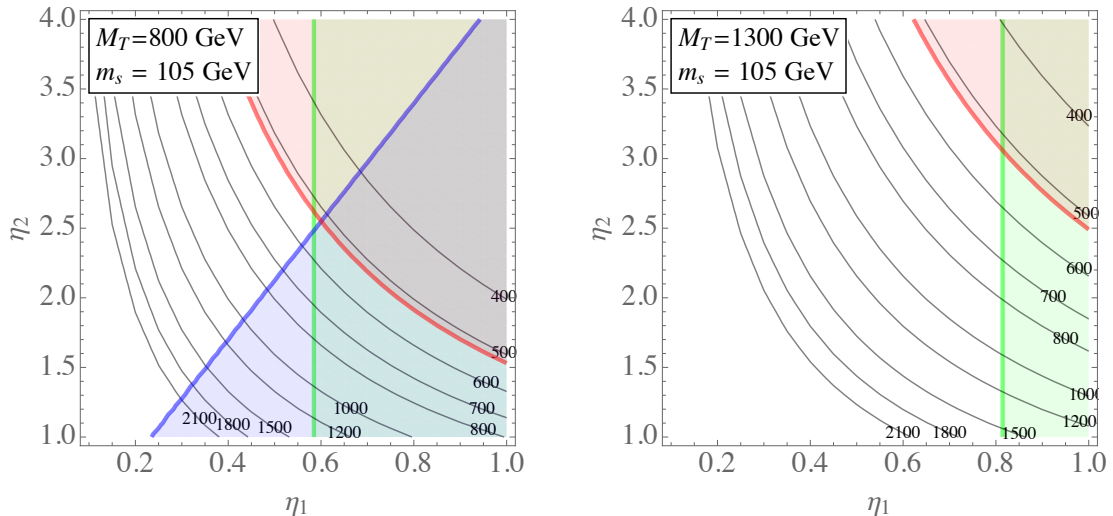


FIG. 3. For selected T and s masses, constraints on η_1 and η_2 from precision electroweak data (green), diphoton resonance searches [70, 71] (red), and searches for vector-like quarks [62] (blue), along with contours of Λ in GeV. The allowed region is unshaded.

a complete description. There are two principal challenges arising from the running of the couplings,

$$\frac{d\eta_2}{d\ln\mu} \simeq \frac{\eta_2^3}{4\pi^2} \quad (12)$$

$$\frac{d\lambda_s}{d\ln\mu} \simeq \frac{9\lambda_s^2}{8\pi^2} - \frac{3\eta_2^4}{2\pi^2} + \frac{\lambda_s\eta_2^2}{2\pi^2} \quad (13)$$

where μ denotes the renormalization scale. The most serious problem is that for large values of η_2 , the self-coupling λ_s is quickly driven to zero, and the scalar potential becomes unstable. The second is that η_2 reaches a Landau pole at somewhat higher scales. The first problem could be ameliorated by coupling additional scalars to s , without impacting our results for EWBG or GWs. For this reason, we do not limit the scope of our investigation based on the running of λ_s . Regarding the second problem, we note that even for $\eta_2 = 3$, the Landau pole is nearly an order of magnitude above M , which we consider to be an acceptably large range of validity for the effective theory.

B. Explicit breaking of Z_2 symmetry

Since we are considering a scenario where the Z_2 symmetry $s \rightarrow -s$ is spontaneously broken during the early universe and restored at the EWPT, domain walls form before the EWPT, and the universe will consist of domains with random signs of the s condensate. The source term for EWBG that arises from Eq. (2) is linear in s , resulting in baryon asymmetries of opposite signs, that could average to zero after completion of the EWPT. To avoid this outcome, the Z_2 symmetry should be explicitly broken, by potential terms

$$V_b = \mu_b s(h^2 - v^2) + \mu'_b s^3 \quad (14)$$

with small coefficients μ_b, μ'_b . We have used the freedom of shifting s by a constant to remove a possible tadpole of s at the true vacuum $(h, s) = (v, 0)$.

The presence of the biasing potential V_b can ameliorate the situation in several ways. First, if the transition to the broken s -phase is of second order, even a small tilt can suffice to make the lower-energy vacuum dominate. Second, in a first order transition, symmetry breaking terms can bias the bubble nucleation rates to prefer the lower-energy vacuum. Indeed, the number of bubbles nucleated during the transition is $n \sim \int_{t_c}^{t_*} dt \Gamma(t)$, where t_* is the time when transition completes, and $\Gamma(t) \sim \exp(-S_3/T)$. Writing the action as $S_{3\pm} = \bar{S}_3 \mp \delta S$ in the two respective vacua, the relative number density of bubbles in each phase at the end of the transition becomes $n_+/n_- \approx \exp(2\delta S_*/T_*)$. In general [74] $S_3 \propto E$, where E is the coefficient of the cubic term in the potential. Using this scaling we may write $\delta S_* = (\delta E/E_0)\bar{S}_3^*$, where typically $\bar{S}_3^*/T_* \approx 100$. In our model $E_0 \approx (3\lambda_s)^{3/2}T/12\pi$, so taking $V_b = \mu_b' s^3$, corresponding to $\delta E = \mu_b'$, and $T_* \approx 100$ GeV, the condition for single-phase vacuum

dominance becomes $\mu_{b'} \gtrsim 0.1\lambda_s^{3/2}$ GeV. Barring very large λ_s , this condition is easily met with no limitations on our analysis.

Even if a domain wall network forms, the higher-energy domains will collapse due to pressure gradients, and we should ensure that this process completes before the EWPT. The collapse starts with the acceleration of a wall at relative position R according to $\ddot{R} = -\Delta V/\tau$, where $\tau \sim \sqrt{\lambda_s}w^3$ is the surface tension (distinct from the tension σ used above in the nucleation estimate), $\Delta V \sim V_b(0, w) \sim \mu u'_b w^3$ is the difference in the vacuum energies, and $w \sim \mu_s/\sqrt{\lambda_s}$ is the singlet VEV. Using $H = 1/2t$ and $T \approx 100$ GeV, one finds that walls reach light speed in time $\delta t/t = \tau H/\delta V \sim 10^{-5}\sqrt{\lambda_s}$ (eV/ $\mu_{b'}$), which is practically instantaneous on the timescales of interest, for reasonable values of $\mu_{b'}$. The higher energy domains subsequently collapse at the speed of light, since there is no appreciable friction. The time required for this process to complete is determined by

$$R_* = 2a(t_1) \int_{t_1}^{t_2} \frac{dt}{a(t)}, \quad (15)$$

where R_* is the comoving size of the domain wall separation. By the Kibble mechanism one expects that $R_* = AH_*^{-1}$ with $A \lesssim 1$, leading to the ratio of domain wall collapse to formation times $t_2/t_1 = (1 + A/2)^2$. The temperature interval corresponding to this time interval is $\Delta T/T \approx A$, assuming that the growth phase also proceeded at the speed of light.

The temperature of the first phase transition, T_1 can be estimated as that when $\partial^2 V/\partial s^2$ becomes negative. In the approximation of neglecting V_b and keeping only leading terms in the high-T expansion one finds $T_1^2 - T_c^2 \sim \lambda_h w_c^2/c_s$ where T_c is the critical temperature of the EWPT, and $c_s = (3\lambda_s + 2\lambda_{hs})/12$. Thus the temperature difference between transitions is of order $\Delta T_{1c} \sim \lambda_h w_c^2/(c_s T_c)$. Requiring that $\Delta T_{1c}/T_c > A$ then gives

$$A < \frac{12\lambda_h}{3\lambda_s + 2\lambda_{hs}} \frac{w_c^2}{T_c^2}. \quad (16)$$

Given that $A \sim (T_*/S_3^*)(\Delta T/T)_* \sim 10^{-2} - 10^{-4}$ [43] this is a very weak constraint. We conclude that it is easy to avoid cosmological problems associated with the domain walls by small symmetry breaking terms which do not affect the rest of our analysis.

III. PHASE TRANSITION AND BUBBLE NUCLEATION

In the examples of interest for this work, the phase transition in the Z_2 -symmetric singlet model proceeds in two steps: starting from the high-temperature global minimum $h = s = 0$, a transition first occurs to nonzero s , while the Higgs field remains at $h = 0$. This is followed by the EWPT, in which s returns to zero and h develops its VEV. The $h^2 s^2$ interaction provides the potential barrier to make this a first order transition.

As usual, the first order transition occurs at the bubble nucleation temperature T_n , which is below the critical temperature T_c , where the two potential minima become degenerate,

$$V_{\text{eff}}(h, s, T_c) \Big|_{\substack{h=0, \\ s=w_c}} = V_{\text{eff}}(h, s, T_c) \Big|_{\substack{h=0, \\ s=0}}, \quad (17)$$

Bubble nucleation occurs when the vacuum decay rate per unit volume Γ_d becomes comparable to H^4 , the Hubble rate per Hubble volume. The decay rate is [75]

$$\Gamma_d \cong T^4 \left(\frac{S_3}{2\pi T} \right)^{3/2} \exp \left(-\frac{S_3}{T} \right), \quad (18)$$

where S_3 is the O(3) symmetric action,

$$S_3 = 4\pi \int r^2 dr \left(\frac{1}{2} \left(\frac{dh}{dr} \right)^2 + \frac{1}{2} \left(\frac{ds}{dr} \right)^2 + V_{\text{eff}} \right). \quad (19)$$

The precise criterion that we use for nucleation is

$$\exp(-S_3/T_n) = \frac{3}{4\pi} \left(\frac{H(T_n)}{T_n} \right)^4 \left(\frac{2\pi T_n}{S_3} \right)^{3/2}, \quad (20)$$

which is satisfied when $S_3/T_n \cong 140$ [76]. We used the package CosmoTransitions [77] to calculate S_3 . The action obtained with the full potential can differ significantly from the commonly used thin wall approximation [78, 79] or the approximation of evaluating it along the minimal integration path for the potential [37]. We compare the predictions for nucleation of these approximations to the full one-loop result, for several exemplary models, in Table III. The approximate methods tend to underestimate the action, giving a higher nucleation temperature; hence we use the values derived from the full one-loop action in the following.

λ_{hs}	m_s (GeV)	$S_3/T _{T=100 \text{ GeV}}$			T_n (GeV)		
		Thin wall	MPP	1-loop	Thin wall	MPP	1-loop
1	120	234	277	427	93.5	92.6	89.8
1.7	200	68.7	101	151	115.6	109.8	100.1
3.2	300	37.9	36.8	54.3	134.3	133.8	121.6

TABLE I. Examples of the dimensionless tunneling action S_3/T , evaluated at $T = 100 \text{ GeV}$, and ensuing nucleation temperatures, computed within the thin wall and minimal potential path (MPP) approximations, compared with the value obtained using the resummed one-loop potential. In there example, $\lambda_s = 1$ and $\Lambda = 540 \text{ GeV}$.

There are two complementary parameters for characterizing the strength of the first order transition. One is the ratio of the Higgs VEV to the temperature at the time of nucleation, v_n/T_n , which is especially relevant for EWBG, as we will discuss in Sect. V B. The other, which is more important for GW production, is the ratio of released vacuum energy density to the radiation energy density [80, 81]:

$$\alpha = \frac{1}{\rho_\gamma} \left(\Delta V - \frac{T_n}{4} \Delta \frac{dV}{dT} \right), \quad (21)$$

where $\rho_\gamma = g_* \pi^2 T_n^4 / 30$, g_* is the effective number of degrees of freedom in the plasma (we use $g_* = 106.75$) and Δ denotes the difference between the unbroken and broken phase. α quantifies the amount of supercooling that occurs prior to nucleation, which determines how much free energy is available for the production of GWs.

IV. WALL VELOCITY AND SHAPE

The derivation of the wall velocity and field profiles is a technically demanding problem [43], that was first addressed in the context of Higgs plus singlet models in Refs. [47, 49, 82], in various approximations. One must solve the equations of motion (EOM) for the scalar sector coupled to a perfect fluid,

$$\begin{aligned} E_h(z) &\equiv -h''(z) + \frac{dV_{\text{eff}}(h, s; T_+)}{dh} + \sum_i N_i \frac{dm_i^2}{dh} \int \frac{d^3 p}{(2\pi)^3 2E} \delta f_i(\vec{p}, z) = 0, \\ E_s(z) &\equiv -s''(z) + \frac{dV_{\text{eff}}(h, s; T_+)}{ds} + \sum_i N_i \frac{dm_i^2}{ds} \int \frac{d^3 p}{(2\pi)^3 2E} \delta f_i(\vec{p}, z) = 0, \end{aligned} \quad (22)$$

where z is the direction normal to the wall, that is to a good approximation planar by the time it has reached its terminal velocity. We use a sign convention where the wall is moving to the left, so that $z > 0$ corresponds to the broken phase. The sum is over all the relevant species coupled to h or s in the plasma, with N_i and m_i respectively denoting the number of degrees of freedom and the field-dependent mass of the corresponding species, and δf_i the deviation from equilibrium of its distribution function. All the temperature-dependent quantities appearing in these equations are evaluated at T_+ , which is the plasma's temperature just in front of the wall. We calculate T_+ in Appendix B using the method described in Ref. [81], and δf_i will be computed in Sect. IV A.

The terms in Eqs. (22) with δf_i represent the friction⁴ of the plasma on the wall, that leads to a terminal wall speed $v_w < 1$, unless the friction is too small and the wall runs away to speeds close to that of light. Following

⁴ The term “friction” is strictly speaking not correct, but we adopt this commonly used terminology. More accurately, the last terms in (22) represent the additional pressure created by the out-of-equilibrium perturbations, which modify the effective action in the same way as the usual thermal excitations.

previous work, we take the dominant sources of friction to be from the top quark ($i = t$) and electroweak gauge bosons ($i = W$), neglecting the contributions to friction from the Higgs itself and from the singlet. This approximation is bolstered by the smaller number of degrees of freedom $N_h = N_s = 1$ compared to $N_t = 12$ and $N_W = 9$, as well as the smallness of the Higgs self-coupling λ_h and the not-too-large values of the cross-coupling λ_{hs} that will be favored in the subsequent analysis. Then the friction term for the s equation of motion vanishes, since s couples only to itself and to the Higgs, apart from its suppressed dimension-5 coupling to t . This allows for some simplification in the following procedure.

In Ref. [54], a similar study of the present model was done, where no *a priori* restriction of the wall shape was assumed, but it was found that the actual shapes conform to a very good approximation to the tanh profiles

$$\begin{aligned} h(z) &= \frac{h_0}{2} [1 + \tanh(z/L_h)], \\ s(z) &= \frac{s_0}{2} [1 - \tanh(z/L_s + \delta)], \end{aligned} \quad (23)$$

where h_0 and s_0 are respectively the vacuum expectation values (VEV) of the h and s fields in the broken and unbroken phases. Hence we adopt the ansatz (23), which allows the singlet and Higgs wall profiles to have different widths, and to be offset from each other by a distance $L_s\delta$. The s field's VEV is taken to be the usual one evaluated at T_+ , which solves the equation $dV_{\text{eff}}(0, s; T_+)/ds|_{s=s_0} = 0$. The situation is more complicated for the h field, for which the Higgs VEV should be evaluated at T_- , the plasma's temperature behind the wall. Since we are fixing a constant temperature T_+ in the potential, the change in the effective action due to the shift in the background temperature must be accounted for by the perturbation in the broken phase. As a consequence we are choosing h_0 so that it solves the equation

$$\left(\frac{dV_{\text{eff}}(h, 0; T_+)}{dh} + \sum_i N_i \frac{dm_i^2}{dh} \int \frac{d^3 p}{(2\pi)^3 2E} \delta f_i(\vec{p}, z) \right) \Big|_{h=h_0, z \rightarrow \infty} = 0. \quad (24)$$

This choice guarantees that the Higgs EOM is satisfied far behind the wall. We will estimate the uncertainty of our results due to this approximation in Sect. VID.

To approximately solve the Higgs EOM, one can define two independent moments $M_{1,2}$ of $E_h(z)$, and assume that they both vanish at the optimal values of v_w and L_h . A convenient choice is [49]

$$M_1 \equiv \int dz E_h(z) h'(z) = 0, \quad (25)$$

$$M_2 \equiv \int dz E_h(z) [2h(z) - h_0] h'(z) = 0. \quad (26)$$

These also have nice physical interpretations that naturally distinguish them as good predictors of the wall speed and thickness, respectively. M_1 is a measure of the net pressure on the wall, so that Eq. (25) can be interpreted as the requirement that a stationary wall should have a vanishing total pressure; nonvanishing M_1 would cause it to accelerate. Therefore one expects that Eq. (25) principally determines the wall speed v_w , while depending only weakly on the thickness L_h . With that sign convention, M_1 can be interpreted as the pressure in front of the wall minus the pressure behind it, so that $M_1 > 0$ corresponds to a net force slowing down the wall. On the other hand, M_2 is a measure of the pressure gradient in the wall. If nonvanishing, it would lead to compression or stretching of the wall, causing L_h to change. Hence Eq. (26) mainly determines L_h , and depends only weakly on v_w . The two equations are approximately decoupled, facilitating their numerical solution. This is illustrated in Fig. 4, which shows the dependence of M_1 and M_2 on v_w and L_h .

We chose a different approach to determine the singlet wall parameters L_s and δ . Instead of solving moment equations analogous to (25,26), one can determine their values by minimizing the s field action

$$\begin{aligned} S(L_s, \delta) &= \int dz \left\{ \frac{1}{2} (s')^2 + [V_{\text{eff}}(h, s, T_+) - V_{\text{eff}}(h, s^*, T_+)] \right\} \\ &= \frac{s_0^2}{6L_s} + \int dz [V_{\text{eff}}(h, s, T_+) - V_{\text{eff}}(h, s^*, T_+)], \end{aligned} \quad (27)$$

with respect to L_s and δ . Here s^* is a field configuration with arbitrary fixed parameters L_s^* and δ^* , that we choose to be $L_s^* = L_h$ and $\delta^* = 0$. The second term is just a constant, but it allows for the convergence of the

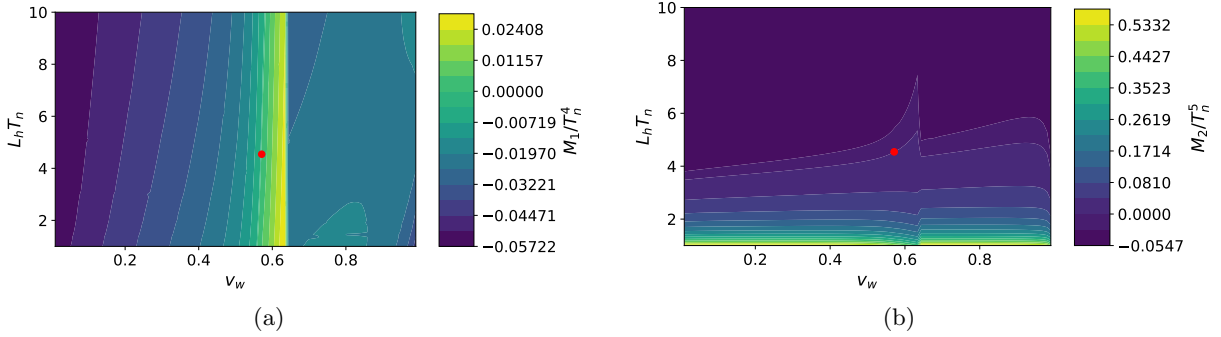


FIG. 4. Moments of the Higgs EOM (a) M_1 and (b) M_2 as a function of the wall velocity v_w and the Higgs wall width L_h for a model with parameters $\lambda_{hs} = 1$, $\lambda_s = 1$ and $m_s = 130$ GeV. The red dot is the solution of Eqs. (25,26). As expected, M_1 is roughly independent of L_h while M_2 depend mainly on L_h . The moments are discontinuous at $v_w \approx 0.63$ because this corresponds (for this specific model) to the boundary between hybrid and detonation walls, where v_+ and T_+ are discontinuous.

integral by canceling the contributions of V_{eff} at $z \rightarrow \pm\infty$. This method has the advantage that it does not depend on any arbitrary choice of moments, and it is more efficient to numerically minimize the function of two variables than to solve the system of equations for the moments of the EOMs.

A. Transport equations for fluid perturbations

The final step toward the complete determination of the velocity and the shape of the wall is to compute the distribution functions' deviations from equilibrium δf_i , by solving the Boltzmann equation for each relevant species in the plasma. The method of approximating the full Boltzmann equation by a truncated set of coupled fluid equations was originally carried out in Ref. [43], for the regime of slowly-moving walls (see also Ref. [49]). This approach was recently improved in Ref. [56] in order to be able to treat wall speeds close to or exceeding the speed of sound consistently. We briefly summarize the formalism, which has been adopted for the present study.

The out-of-equilibrium distribution function can be parametrized in the wall frame as

$$f = \frac{1}{\exp[\beta\gamma(E - v_+ p_z)(1 - \delta\tau) - \mu] \pm 1} + \delta f_u, \quad (28)$$

where $\beta = 1/T_+$ and the \pm is $+$ for fermions and $-$ for bosons. $\delta\tau$ and μ are the dimensionless temperature and chemical potential perturbations from equilibrium, and δf_u is a velocity perturbation whose form is unspecified, but is constrained by $\int d^3 p \delta f_u = 0$. By assuming that the perturbations are small, one can expand f to linear order in μ , $\delta\tau$ and the velocity perturbation δf_u to obtain

$$\delta f \approx \delta f_u - f'[\mu + \beta\gamma\delta\tau(E - v_+ p_z)], \quad (29)$$

with

$$f' = \frac{d}{dX} \frac{1}{e^X \pm 1} \bigg|_{X=\beta\gamma(E - v_+ p_z)}. \quad (30)$$

To simplify the problem, one models the plasma as being made of three different species: the top quark, the W bosons (shorthand for W^\pm and Z) and a background fluid, which includes all the remaining degrees of freedom. It is convenient to write the velocity perturbation as $u \propto \int d^3 p (p_z/E) \delta f_u$ when constructing the moments of the linearized Boltzmann equation. By taking three such moments, using the weighting factors 1, E and p_z/E , the perturbations are determined by transport equations

$$Aq' + \Gamma q = S, \quad (31)$$

$$q'_{\text{bg}} = -\tilde{A}_{\text{bg}}^{-1}(\Gamma_{\text{bg},t} q_t + \Gamma_{\text{bg},w} q_w), \quad (32)$$

where prime denotes d/dz , $q_i = (\mu_i, \delta\tau_i, u_i)^\top$, $q = (q_w^\top, q_t^\top)^\top$, the Γ matrices are collision terms, and S is the source term, whose definitions, as well as those of the the matrices A , Γ , $\tilde{A}_{\text{bg}}^{-1}$, $\Gamma_{\text{bg},t}$, $\Gamma_{\text{bg},w}$, can be found in Ref. [56]. If A and Γ were independent of z , one could use the Green's function method to solve Eq. (31); however, A is a function of $m_i(z)/T$. To deal with this dependence on z , we discretize space, $z \rightarrow z_0 + n\Delta z$ with $n = 0, \dots, N-1$, and Fourier transform Eq. (31),

$$\frac{2\pi i}{\Delta z} \left(\frac{k}{N} - \left\lfloor \frac{2k}{N} \right\rfloor \right) \tilde{q}_k + \frac{1}{N} \sum_{l=0}^{N-1} (\widetilde{A^{-1}\Gamma})_{(k-l) \bmod N} \tilde{q}_l = (\widetilde{A^{-1}S})_k, \quad k = 0, \dots, N-1, \quad (33)$$

where the tilde denotes the discrete Fourier transform. This is a linear system that is straightforward to numerically solve for \tilde{q}_k . Once \tilde{q}_k is known, it can be transformed back and interpolated to obtain $q(z)$. Eq. (32) can then be integrated using a Runge-Kutta algorithm.

Finally, one can substitute Eq. (29) into the Higgs EOM (22) to express the friction in terms of the fluid perturbations μ_i , $\delta\tau_i$ and u_i . This leads to the result

$$\int \frac{d^3p}{(2\pi)^3 2E} \delta f_i = \frac{T_\perp^2}{2} \left[C_0^{1,0} \mu_i + C_0^{0,0} (\delta\tau_i + \delta\tau_{\text{bg}}) + D_v^{0,-1} (u_i + u_{\text{bg}}) \right], \quad (34)$$

where the functions $C_v^{m,n}$ and $D_v^{m,n}$ can be found in Ref. [56].

V. COSMOLOGICAL SIGNATURES

We have now established the machinery needed to compute all the relevant properties of the first order phase transition bubbles, starting from the fundamental parameters of the microscopic Lagrangian. In this section we describe how to apply these results for the estimation of GW spectra and the baryon asymmetry.

A. Gravitational Waves

We follow the methodology of Refs. [7, 81, 83] to estimate future gravitational wave detectors' sensitivity to the GW signals that can be produced by a first-order electroweak phase transition in the models under consideration. The GW spectrum $\Omega_{\text{gw}}(f)$ is the contribution per frequency octave to the energy density in gravitational waves, *i.e.*, $\int \Omega_{\text{gw}} d\ln f$ is the fraction of energy density compared to the critical density of the universe. The spectrum gets separate contributions from the scalar fields, sound waves in the plasma and magnetohydrodynamical turbulence created by the phase transition:

$$\Omega_{\text{gw}}(f) = \Omega_\phi(f) + \Omega_{\text{sw}}(f) + \Omega_{\text{m}}(f), \quad (35)$$

Each of these contributions depends on the wall velocity v_w , the supercooling parameter α (Eq. (21)), and the inverse duration of the phase transition, defined as

$$\beta = H(T_n) T_n \left. \frac{d}{dT} \frac{S_3}{T} \right|_{T=T_n}. \quad (36)$$

Another useful quantity is the mean bubble separation, which can be written in terms of v_w and β as [7]

$$R = \frac{(8\pi)^{1/3}}{\beta} \max[c_s, v_w]. \quad (37)$$

It has been shown in Ref. [50] that interactions with gauge bosons prevent the wall from running away indefinitely towards $\gamma \rightarrow \infty$. In that case, the contribution from the scalar fields has been shown to be negligible. Furthermore, the estimates for the magnetohydrodynamical turbulence are very uncertain and sensitive on the details of the phase transition dynamics [84] and are expected to be much smaller than the contribution from sound waves. Hence, we consider only the effects from the latter and set $\Omega_{\text{m}}(f) = \Omega_\phi(f) = 0$. For convenience, we reproduce the numerical fits of the GW spectrums derived in Refs. [7, 81, 83] in appendix C.

We will use these predictions with respect to four proposed space-based GW detectors: LISA [85], AEDGE [11], BBO [86] and DECIGO [9]. A successful GW detection depends upon having a large enough signal-to-noise ratio [87],

$$\text{SNR} = \sqrt{\mathcal{T} \int_{f_{\min}}^{f_{\max}} df \left[\frac{\Omega_{\text{gw}}(f)}{\Omega_{\text{sens}}(f)} \right]^2} \quad (38)$$

where $\Omega_{\text{sens}}(f)$ denotes the sensitivity of the detector⁵ and \mathcal{T} is the duration of the mission. The sensitivity curves for the detector LISA, BBO and DECIGO were obtained from Ref. [88]. Whenever SNR is greater than a given threshold SNR_{thr} , we conclude that the signal can be detected. In general, this threshold can depend upon the configuration of the detector. For all the experiments, we take $\text{SNR}_{\text{thr}} = 10$ and $\mathcal{T} = 1.26 \times 10^8$ s. In the following, SNR_{max} will designate the maximum signal-to-noise ratio detected by one of the detectors:

$$\text{SNR}_{\text{max}} \equiv \max[\text{SNR}_{\text{LISA}}, \text{SNR}_{\text{AEDGE}}, \text{SNR}_{\text{BBO}}, \text{SNR}_{\text{DECIGO}}]. \quad (39)$$

While $\Omega_{\text{sens}}(f)$ can be obtained from the noise spectrum of a detector, it is not practical to compare it to the GW spectrum directly; one needs to compute the SNR to determine if signal is detectable. A useful tool for visualizing the sensitivity of a detector is the power-law sensitivity curve (PLS) [89], defined as the envelope of the set of power-law curves, $\Omega_{\text{gw}} = af^b$, that generate a SNR of SNR_{thr} when observed over a duration \mathcal{T} . By construction, every power-law curve above the PLS has $\text{SNR} > \text{SNR}_{\text{thr}}$ and can therefore be detected.

B. Baryogenesis

The mechanism of electroweak baryogenesis is sensitive to the speed and shape of the bubble wall during the phase transition. In most previous studies, these quantities were treated as free parameters to be varied, but in this work we have already derived them, as was discussed in Section IV.

An important requirement for EWBG is to avoid the washout, by baryon-violating sphaleron interactions, of the generated asymmetry inside the bubbles of broken phase, once they have formed. This leads to the well-known constraint [90]

$$\frac{v_n}{T_n} > 1.1 \quad (40)$$

which was derived within the SM for low Higgs masses where a first order EWPT was possible. The bound can be slightly higher (up to 1.2) in singlet-extended models [91], depending upon the parameters, due to the sphaleron energy being modified. Here we adopt the SM constraint (40); we checked that taking the more stringent constraint 1.2 removes $\sim 5\%$ of viable models in the scan over parameter space to be described below.

Near the bubble wall, CP-violating processes associated with the effective interaction in Eq. (2) give rise to perturbations of the plasma, that result in a local chemical potential μ_{B_L} for left-handed baryons, which by imposing the chemical equilibrium of strong-sphaleron interactions, is related to those of the t_L , t_R^c and b_L quarks by

$$\mu_{B_L} = \frac{1}{2} (1 + 4K_1^t) \mu_t + \frac{1}{2} (1 + 4K_1^b) \mu_b - 2K_1^t \mu_{t^c}, \quad (41)$$

where K_1^a -functions were defined in [92] ($K_1^a = D_0^a$ in the notation of [55]). The μ_{B_L} potential biases sphalerons, leading to baryon number violation, whose associated Boltzmann equation can be integrated to obtain the baryon to photon ratio⁶

$$\eta_b = \frac{405 \Gamma_{\text{sph}}}{4\pi^2 v_w \gamma_w g_* T} \int dz \mu_{B_L} f_{\text{sph}} e^{-45\Gamma_{\text{sph}}|z|/4v_w} \quad (42)$$

where f_{sph} quantifies the diminution of the sphaleron rate in the broken phase [93].

⁵ For AEDGE, we use the envelope of minimal strain that can be achieved by each resonance, with its width scaled to approximate $\Omega_{\text{sens}}(f)$. This curve is expected to reproduce the correct SNR up to about 10%.

⁶ The extra factor of $\gamma_w = 1/\sqrt{1 - v_w^2}$ in the denominator was pointed out by Ref. [55].

The most challenging step for the computation of EWBG is in the determination of the chemical potentials μ_{t_L} , $\mu_{t_R^c}$ and μ_{b_L} appearing in Eq. (41). They satisfy fluid equations resembling the network (31,32), except that the potentials relevant for EWBG are CP-odd, whereas those determining the wall profiles are CP-even.

The CP-odd transport equations have been discussed extensively in the literature, leading to two schools of thought as to how best to compute the source term for the CP asymmetries. These are commonly known as the VEV-insertion [94, 95] or WKB (semiclassical) [96–101] methods, respectively. A detailed discussion and comparison of the two approaches was recently given in Ref. [55], which quantified the well-known fact that the VEV-insertion source tends to predict a larger baryon asymmetry than the WKB source, by a factor of ~ 10 . In the present work we adopt the WKB approach, which was updated in Ref. [55] to allow for consistently treating walls moving near or above the sound speed. In addition, that reference computed the source term arising from the same effective interaction (2) as in the present model, so we can directly adopt the CP-odd fluid equations studied there.

VI. MONTE CARLO RESULTS

In order to study the properties of the phase transition, we performed a scan over the parameter space of the models, imposing several constraints. We found that variations in λ_s do not qualitatively change the results, prompting us to initially fix its value at $\lambda_s = 1$, leaving λ_{hs} and m_s as the free scalar potential parameters. We will first discuss this slice of parameter space, and later consider the quantitative dependence on λ_s . We also chose $\Lambda = 540$ GeV, which is conservative since there are no collider constraints on its value for singlet masses in the region $m_s = [110, 160]$ GeV. Recall that Λ is important for the determination of the baryon asymmetry η_b , which is expected to scale roughly as $1/\Lambda$. Finally, in order to prevent Higgs invisible decays, we imposed $m_s > m_h/2$.

We used a Markov Chain Monte Carlo algorithm to efficiently explore the regions of parameter space having desired phase transition properties. Starting with an initial model satisfying the sphaleron bound (40), one generates a new trial model by randomly varying the parameters λ_i by small increments δ_i . The trial model is added to the chain using a conditional probability

$$P = \min \left[\frac{v_n/T_n}{1.1}, 1 \right] \quad (43)$$

that favors models having strong first order phase transitions, and for which a solution to the nucleation condition (20) can be found. We adjust the δ_i so that roughly half of the models are kept, with larger values of δ_i being more likely to result in a rejection.

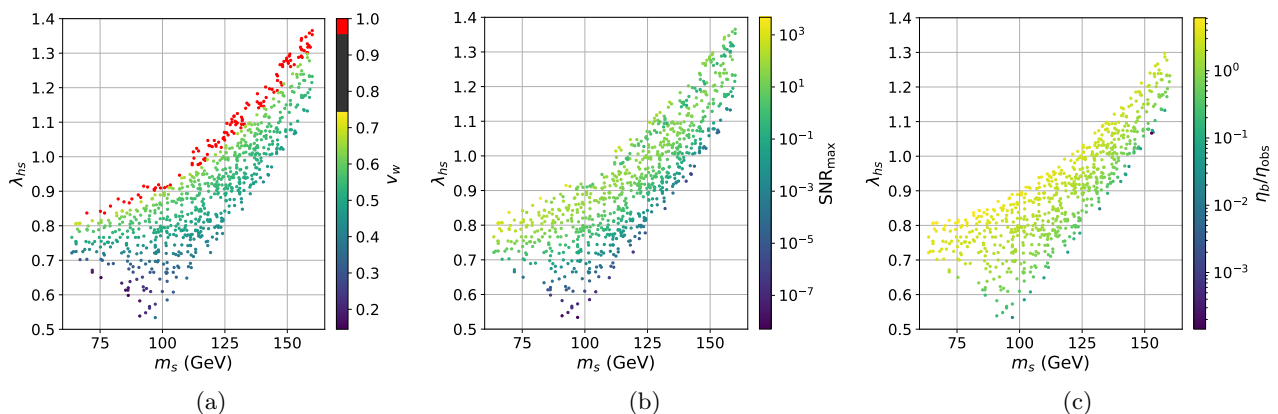


FIG. 5. Scan of the parameter space with $\lambda_s = 1$ and $\Lambda = 540$ GeV. The colors represent (a) the terminal wall velocity v_w , (b) the maximum signal-to-noise ratio of gravitational waves that could be detected by either LISA, AEDGE, BBO or DECIGO and (c) the baryon asymmetry (in units of the observed value) produced by the phase transition. The red dots in (a) correspond to detonation solutions with $v_w \approx 1$, and the latter are not included in (c) since they are expected to produce a negligible baryon asymmetry.

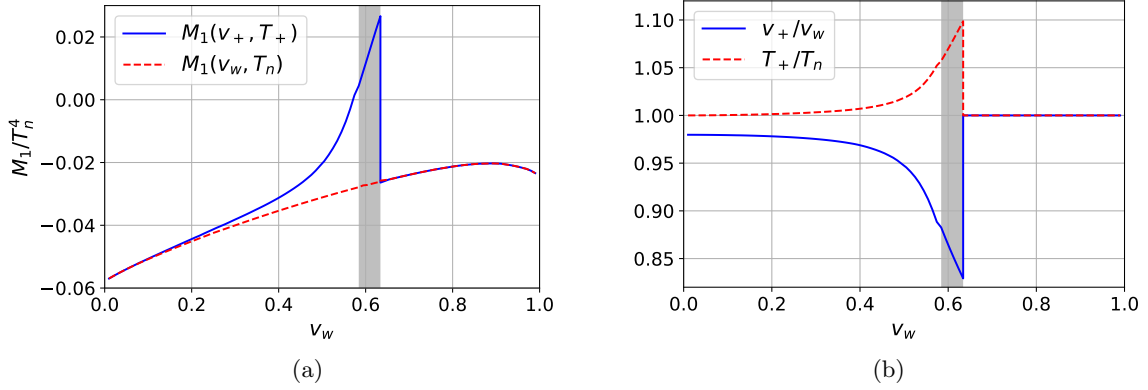


FIG. 6. Left (a): Pressure on the wall M_1 as a function of the wall velocity v_w . The solid (dashed) line corresponds to the pressure evaluated at the velocity v_+ (v_w) and the temperature T_+ (T_n). Right (b): Relation between the naive variables v_w , T_n and the ones relevant for evaluating M_1 , namely v_+ and T_+ . Both plots were obtained using the parameters $m_s = 130$ GeV, $\lambda_{hs} = \lambda_s = 1$ and $L_h = 5/T_n$. The shaded region corresponds to hybrid wall solutions characterized by $c_s < v_w < \xi_J$.

This procedure yielded 833 models with strong phase transitions, of which 708 were amenable to finding solutions for the moment equations (25-26). Our analysis is expected to hold for $\gamma \lesssim 10$. Above that bound, our algorithm becomes numerically unstable which prevents it from giving any trustworthy result. It is therefore impossible to determine the type of solution of the 125 remaining models using our method alone: they could either stabilize at an ultra-relativistic speed satisfying $10 \lesssim \gamma < \infty$, or run away indefinitely towards $\gamma \rightarrow \infty$. The value of the baryon asymmetry should not be affected by this ambiguity since it is negligible for $v_w \approx 1$. However, the GW spectrum produced during the phase transition is sensitive to the type of solution since runaway walls have a non-negligible fraction of their energy stored in the wall, while for non-runaway walls, the energy gets dissipated into the plasma, so the fraction of energy in the wall becomes negligible. This ambiguity can be lifted using the result of Ref. [50], which found that in the limit $\gamma \rightarrow \infty$, interactions between gauge bosons and the wall create a pressure proportional to γ , preventing it from running away⁷. We can therefore assume that the 125 models without a solution to the moment equations (25-26) correspond to non-runaway walls with $v_w \approx 1$.

The results of this scan, showing the calculated wall velocity, signal-to-noise ratio of gravity waves observable by at least one of the proposed experiments (LISA, AEDGE, BBO or DECIGO), and the predicted baryon asymmetry (in units of the observed value) are presented in Fig. 5, in the plane of λ_{hs} versus m_s .

A. Deflagration versus detonation solutions

A striking feature of these results is that all the detonation solutions have $v_w \approx 1$.⁸ We have tested that this is not specific to our choice of fixed parameter values, but also holds for all models having $0.01 < \lambda_s < 8$ and $\Lambda > 110$ GeV; hence it seems to be a general property of phase transitions in the Z_2 -symmetric singlet framework. One can understand this behavior by considering the net pressure opposing the wall's expansion, M_1 (recall Eq. (25-26)), as a function of the wall velocity, as illustrated in Fig. 6. It shows how M_1 differs when evaluated with the appropriate quantities v_+, T_+ rather than the incorrect ones v_w, T_n . Using the latter, we would find no solution to the equation $M_1 = 0$ for the exemplary model used in Fig. 6, and would then incorrectly conclude that it satisfies $v_w \approx 1$. The relevant quantities are those measured right in front of the wall, v_+ and T_+ . The speed v_+ is smaller than v_w for $v_w < \xi_J$, which would lower the pressure against the wall (ξ_J is the Jouguet velocity, defined as the smallest velocity a detonation solution can have). However, in the same region, the temperature T_+ is larger than T_n , which causes the pressure to increase. The latter effect turns out to dominate over the former. Indeed, the actual pressure, represented by the solid blue line in Fig. 6, increases much more rapidly than

⁷ More recently, the authors of Ref. [51] have carried out an all-orders resummation at leading-log accuracy, finding that the pressure is in fact proportional to γ^2 for fast-moving walls.

⁸ Strictly speaking there are models with $v_w < 1$ detonation solutions but these always have another solution at a lower velocity corresponding to a deflagration or hybrid wall. We only consider the latter because in a realistic situation, the bubble is created at $v_w = 0$ and accelerates until it reaches the solution with the lowest velocity.

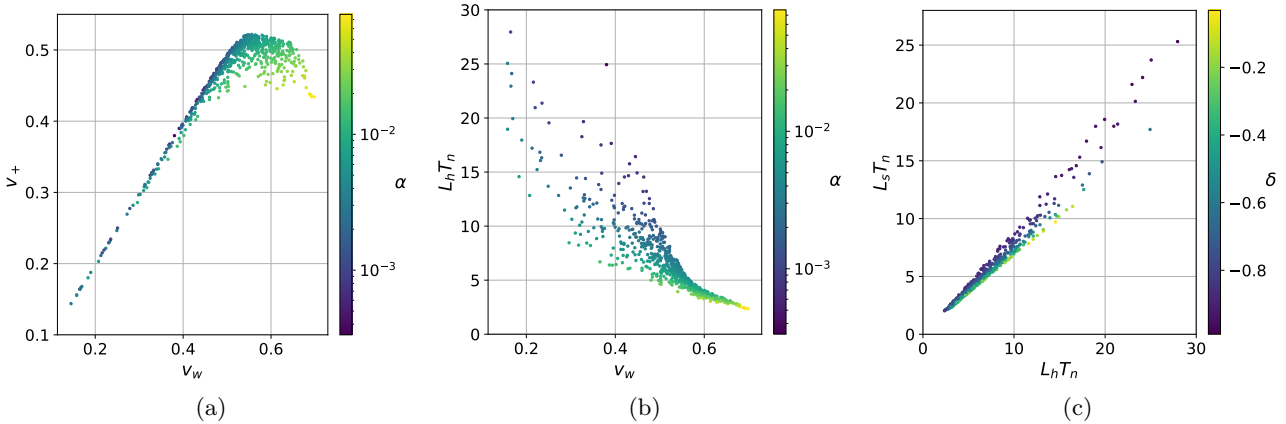


FIG. 7. Shape and velocity of the deflagration solutions. (a) Correlation between the wall velocity v_w and the fluid velocity in front of the wall, v_+ ; (b) dimensionless wall width $L_h \times T_n$ versus v_w ; and (c) correlation of the s and h wall widths. Colors indicate the supercooling parameter α (Eq. (21)) in (a,b), or the wall offset δ (Eq. (23)) in (c).

$M_1(v_w, T_n)$ close to the speed of sound. This qualitative difference allows for a solution to $M_1 = 0$, which would have been missed if we had used the naive quantities v_w and T_n .

We find that the previous statements apply quite generally: for all models, $T_+ > T_n$ when $v_w < \xi_J$, and this always leads to a much higher pressure on the wall, even if the difference between T_+ and T_n is quite small; the pressure barrier at $v_w = \xi_J$ is always greater than the maximum possible value for a detonation solution. Therefore, if the phase transition is strong enough to overcome the pressure barrier at ξ_J , the solution becomes a detonation, but the pressure in the region $v_w > \xi_J$ is never enough to prevent it from accelerating towards $v_w \approx 1$. If the phase transition is weaker, the pressure barrier is high enough to impede the detonation, and it becomes a deflagration or hybrid solution.

The wall thickness and speed for the models with deflagration⁹ solutions are shown in Fig. 7, which demonstrates that the behaviors for subsonic (deflagration) and supersonic (hybrid) walls are rather different. Subsonic walls generally have $v_+ \approx v_w$, which is expected since the fluid should not be strongly perturbed by a slowly moving wall. The wall width is not uniquely determined by v_w , but there exists a clear correlation, with slower walls being thicker. For supersonic cases, the correlation between v_+ and v_w gets inverted: higher wall velocity leads to lower v_+ . The wall width becomes uniquely determined by v_w and the relation between these two variables is to a good approximation linear. One observes that stronger phase transitions, quantified by higher values of α , generally produce faster and thinner walls. Even for the strongest transitions our walls still have thickness $LT \gtrsim 3$. Since the semiclassical force mostly affects particles with momenta $\langle k_z \rangle \sim T$, we find $L\langle k_z \rangle \gtrsim 3$, so that the semiclassical approximation is still valid. In fact the semiclassical picture has been shown to remain valid for surprisingly narrow walls [102], working very well for $L\langle k_z \rangle \approx 4$ and still reasonably for $L\langle k_z \rangle \approx 2$. There is a linear correlation between the h and s wall widths, but the slope is not 1; in all cases, we find that $L_h > L_s$. The distribution of wall offset values δ is also indicated in Fig. 7(c).

B. Baryogenesis and gravity wave production

Of the 833 sampled models, 513 are able to generate the baryon asymmetry at a level large enough to agree with observations, and 321 can produce observable gravitational waves. More detailed results are presented in Table II. The complementarity of the experiments considered here, with respect to the present model, can be appreciated by considering the relation between the maximum GW amplitude $\max[\Omega_{\text{gw}} h^2]$ and the frequency of this peak amplitude f_{max} , as shown in Fig. 8(a). While a large fraction of the models are above BBO's and DECIGO's PLS, the peak frequency of the strongest detonation walls are positioned exactly in LISA's region of

⁹ Henceforth we take “deflagration” to also include hybrid solutions

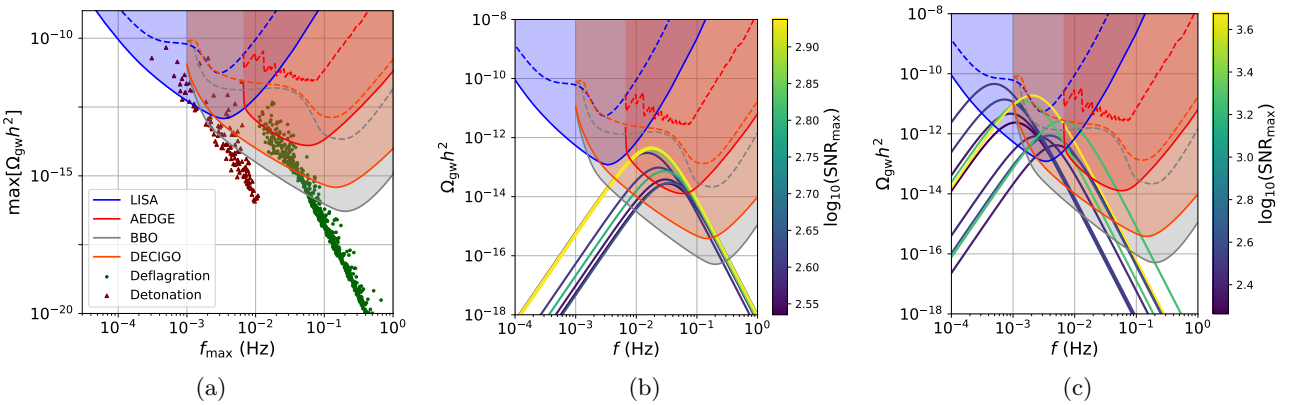


FIG. 8. (a): Maximum amplitude of GW as a function of the peak frequency f_{max} with the PLS (solid line) and the sensitivity $\Omega_{\text{sens}} h^2$ (dashed line) of the four considered detectors. (b) and (c): Spectrum of GW produced by the 10 models with the highest SNR_{max} for (b) deflagration and (c) detonation solutions.

maximal sensitivity, and the same is true for the deflagration walls and three other detectors. Consideration of the complete spectrum's shape, shown in Fig. 8 (b,c) for deflagration and detonation solutions respectively, shows that even if the detonation spectrum peaks in LISA's, BBO's and DECIGO's PLS, the tail of the distribution can be above that of AEDGE. This implies that detonation walls can be probed by all the detectors, while only AEDGE, BBO and DECIGO can efficiently observe deflagration walls.

In previous studies, where the wall velocity was considered as a free parameter, there was an expectation that baryogenesis would be less efficient with increasing v_w , whereas gravity waves would become more so. In the present study, where v_w is not adjustable but is a derived parameter, we surprisingly find that rather than EWBG and observable GWs being anticorrelated, instead they are positively correlated, as is illustrated in Fig. 9 (a). This can be understood from the fact (see Fig. 7 (b)) that L_h is a decreasing function of v_w , which enhances EWBG. Moreover, the relevant velocity for EWBG is v_+ , which is a decreasing function of v_w for supersonic walls, and is bounded by $v_+ < c_s$; this effect also enhances EWBG for fast-moving walls. The actual relation between η_b and v_w is shown in Fig. 9 (b) and, at least for supersonic walls, there is a positive correlation between these two variables, which results in models having both high GW production and baryon asymmetry. Fig. 9 also indicates that supercooling parameter α is positively correlated with both η_b and SNR_{max} : stronger phase transitions generally lead to both higher GW and baryon production.

Detailed predictions for EWBG in the Z_2 symmetric model were previously made in Refs. [37] and [29], as opposed to merely requiring the sphaleron bound (40) to be satisfied. Comparisons with the present work are hindered by the fact that different source terms for the CP asymmetry were assumed. In Ref. [37], the dimension-6 coupling $i(y_t/\sqrt{2})(s/\Lambda)^2 \bar{h} t_L t_R$ was used, rather than the dimension-5 coupling in Eq. (2). Moreover, a value $v_w = 0.2$ was taken for the wall velocity, and an estimate $L_h = v_n/\sqrt{8V_b}$ was made for the wall width, where v_n is the Higgs VEV at the nucleation temperature, and V_b is the potential barrier between the two minima. For the same potential parameters ($\lambda_s = 0.1$) as in [37], we find no values of v_w below 0.43, and our determination of L_h is two to three times larger than the estimate in [37]. Both of these discrepancies would lead to overestimating the efficiency of EWBG, helping to explain why Ref. [37] obtains a high frequency of successful models, despite the extra suppression that should result from using a dimension-6 source term.

In Ref. [29], the dimension-5 coupling to leptons rather than the top quark was studied, and a different formalism (the VEV insertion approximation) for computing the CP asymmetry was employed, which tends to give significantly larger estimates for the baryon asymmetry than the WKB method that we adopt [55]. Ref. [29] also used a different prescription for resumming thermal masses, which relies upon a high-temperature expansion for the thermal self-energies, and different renormalization conditions. For the same parameters as in the benchmark models given there, we do not find the right pattern of symmetry breaking for the phase transitions, further impeding meaningful comparisons of our respective results.

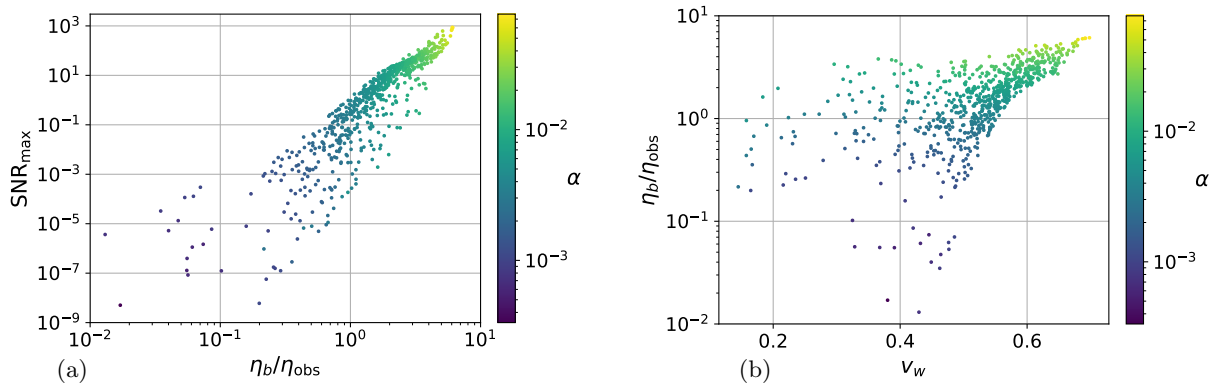


FIG. 9. (a): Relation between the SNR_{max} and the baryon asymmetry produced by the phase transition. (b): Baryon asymmetry as a function of the wall velocity. Both plots only show the deflagration models.

C. Dependence on λ_s and Λ

To study the quantitative dependence on the singlet self-coupling λ_s , we performed 3 other scans similar to the one previously described, taking $\lambda_s = 0.01, 0.1$ and 8 (the largest value being near the limit of perturbative unitarity) and $\Lambda = 540$ GeV. The results of these scans are summarized in Table II. We find that detonation (deflagration) walls are able to produce observable GW when $\lambda_s \gtrsim 0.01$ (0.1), while EWBG remains efficient for $\lambda_s \gtrsim 0.1$. These results confirm that LISA would only be suitable for probing detonation walls¹⁰, which are not good candidates for EWBG. The three other detectors would be sensitive to both types of solutions. Increasing λ_s generally leads to stronger phase transitions, resulting in more models with successful EWBG and detectable GWs.

The value of Λ (recall Eq. (4)) can in principle also have an effect on the strength of the phase transition, through the effective potential's dependence on the top quark mass. The leading thermal term added to the potential varies like $h^2 s^2 T^2 / \Lambda^2$, which becomes negligible at high Λ , but could significantly modify the behavior of the phase transition for $\Lambda \sim T_n$, resulting in a larger baryon asymmetry and GW production. We have verified that this term is already subdominant when $\Lambda = 540$ GeV. However, for $m_s > 110$ GeV, the weaker constraints allow for values of Λ as low as 300 GeV, which could have an important effect on the phase transition.

To test the sensitivity to lower values of Λ , we repeated the previous scans using $\Lambda = \Lambda_{\text{min}}(m_s)$, where Λ_{min} is given by

$$\Lambda_{\text{min}}(m_s) = \begin{cases} 540 \text{ GeV}, & m_s < 110 \text{ GeV} \\ 300 \text{ GeV}, & 110 \text{ GeV} < m_s < 160 \text{ GeV} \end{cases} \quad (44)$$

The results are shown in Table II¹¹. As one could anticipate from the relation $\eta_b \sim 1/\Lambda$, EWBG is more efficient at lower values of Λ . One can also see that the number of detonation walls or walls generating detectable GW does not change substantially, which indicates that the lower values of Λ do not change the character of the phase transition.

D. Theoretical uncertainties

In Ref. [56], the integrals that determine the collision rates Γ appearing in the Boltzmann equation network (31-32) were reevaluated, and it was noticed that the leading log approximation that was used in their derivation leads to theoretical uncertainties of $\mathcal{O}(1)$ in the fractional error. To study the impact of these uncertainties on our results, we recomputed the wall velocity with uniformly rescaled collision rates, $\Gamma \rightarrow 2\Gamma$ and $\Gamma \rightarrow \Gamma/2$. The ensuing variations of velocity Δv and wall width ΔL are shown in Figs. 10 (a) and (b) respectively. The effect

¹⁰ No deflagration solutions with $\text{SNR}_{\text{LISA}} > 10$ were found in the scans presented in Table II.

¹¹ The $\lambda_s = 0.01$ scan is omitted since all accepted models satisfy $m_s < 110$ GeV, making the results identical to those of the previous scan.

Λ	λ_s	$\eta_b/\eta_{\text{obs}} > 1$	Deflagration				Detonation				
			Total	SNRAEDGE > 10	SNRBBO > 10	SNRDECIGO > 10	Total	SNRLISA > 10	SNRAEDGE > 10	SNRBBO > 10	SNRDECIGO > 10
540 GeV	0.01	0	19.5	0	0	0	80.5	3.84	0	7.33	3.49
	0.1	10.1	47	0	5.65	1.78	53	1.09	0	1.78	1.09
	1	$61.6_{+4.6}^{-5.6}$	$85_{+1.5}^{-2.4}$	$4.56_{+0.48}^{-0.36}$	$32.2_{-1.7}^{+0.36}$	$17.2_{+0.34}^{+0.6}$	$15_{-1.5}^{+2.4}$	3.12_0^0	0.6_0^0	$6.36_{-0.12}^0$	$3.84_{-0.12}^0$
	8	76.2	76.5	14.4	45.4	31.2	23.5	7.31	2.97	11.4	9.79
Λ_{min}	0.1	21.6	50.7	0	11.4	3.28	49.3	2.19	0.2	4.87	2.68
	1	70.1	82.5	3.21	31.4	16.3	17.5	4.05	0.28	7.96	5.59
	8	86.56	87	19.4	53.9	40.1	13	6.46	3.95	11.7	10.1

TABLE II. Statistics from the scans performed with $\lambda_s = 0.01, 0.1, 1, 8$ and $\Lambda = 540$ GeV and Λ_{min} . Each entry corresponds to the percentage of models satisfying the indicated constraint. In the row for $\lambda_s = 1$ and $\Lambda = 540$ GeV, the exponents (indices) correspond to the error obtained by substituting the collision matrix Γ for 2Γ ($\Gamma/2$). Λ_{min} is the minimum value of Λ allowed by laboratory constraints.

on v_w can be significant for slow walls, leading to a $\pm 40\%$ change when $v_w \sim 0.2$. On the other hand for nearly supersonic walls, $v_w \gtrsim c_s$, the wall speed is quite insensitive to Γ . The variation of L_h is generally below 5%, much smaller than the corresponding variation in Γ .

This behavior is not surprising since, near the speed of sound, the pressure on the wall is mainly determined by the variation of T_+ , which does not depend on Γ . Likewise, the results for the baryon asymmetry and GW production turn out to be relatively robust against variations in Γ . This is demonstrated by the error intervals in the $\lambda_s = 1$ row of Table II. The error on the ratio of models satisfying $\eta_b/\eta_{\text{obs}} > 1$ or $\text{SNR}_i > 10$ is of order 10%, which is much smaller than the range of variation in Γ .

Another source of uncertainty is the discrepancy between the temperatures computed with the Boltzmann equation (see Section IV A) and the conservation of the energy-momentum tensor (see Appendix B). Ideally one should obtain $T_+ = T_{\text{BE}}(z \rightarrow -\infty)$ and $T_- = T_{\text{BE}}(z \rightarrow \infty)$, where $T_{\text{BE}}(z) = T_+(1 + \delta\tau_{\text{bg}}(z))$ is the local temperature calculated with the Boltzmann equation. The first condition is always satisfied since we impose the boundary condition $\delta\tau_{\text{bg}}(-\infty) = 0$, but we fail to recover the second one due to the different approximations made in the two methods. The discrepancy becomes larger as v_w approaches the Jouguet velocity ξ_J , where T_+ increases compared to $T_- \approx T_n$ (see Fig. 6 (b)). On the other hand, $\delta\tau_{\text{bg}}$ does not change significantly in the same region. Hence, we observe an error in the temperature of order $\Delta T = T_- - T_{\text{BE}}(\infty) \approx T_- - T_+$.

Since the temperature is not accurate in the broken phase, the Higgs EOM is not automatically satisfied asymptotically. To solve that problem, we shift the actual Higgs VEV h_- evaluated in the broken phase by an amount $-\Delta h$, so that the adjusted VEV $h_0 = h_- - \Delta h$ asymptotically solves the EOM (see Eq. (24)). This gives an additional source of uncertainty for v_w and L_h .

We estimate the errors induced on v_w and L_h by ΔT and Δh , assuming they are small enough to justify keeping just the first order terms. Assuming that v_w is completely determined by the solution of $M_1 = 0$ and L_h by $M_2 = 0$, the error on these solutions can be obtained by expanding around the estimated values. For example, for the error in the wall velocity is estimated by

$$0 = M_1(v_w + \Delta v, h_0 + \Delta h, T(z) + \Delta T(z)) \approx M_1(v_w, h_0, T(z)) + \frac{\partial M_1}{\partial v_w} \Delta v + \int dz \frac{\partial M_1}{\partial T(z)} \Delta T(z) + \Delta h M_1, \quad (45)$$

where $\Delta_h M_1 = M_1(v_w, h_0 + \Delta h, T) - M_1(v_w, h_0, T)$, and we integrate over the temperature variation because M_1 is a functional of $T(z)$. Since v_w is the solution of $M_1(v_w, h_0, T(z)) = 0$, the absolute errors on v_w and L_h are estimated as

$$\begin{aligned} |\Delta v| &\approx (|\Delta_T M_1| + |\Delta_h M_1|) \left| \frac{\partial M_1}{\partial v_w} \right|^{-1}, \\ |\Delta L| &\approx (|\Delta_T M_2| + |\Delta_h M_2|) \left| \frac{\partial M_2}{\partial L} \right|^{-1}, \end{aligned} \quad (46)$$

where $\Delta_T M_i = \int dz (\delta M_i / \delta T(z)) \Delta T(z)$. Notice that Eq. (46) overestimates the errors since $\Delta_T M_i$ and $\Delta_h M_i$ have opposite signs. From Eqs. (22,25,26), one can see that the functional derivative $\delta M_i / \delta T(z)$ can be approximated

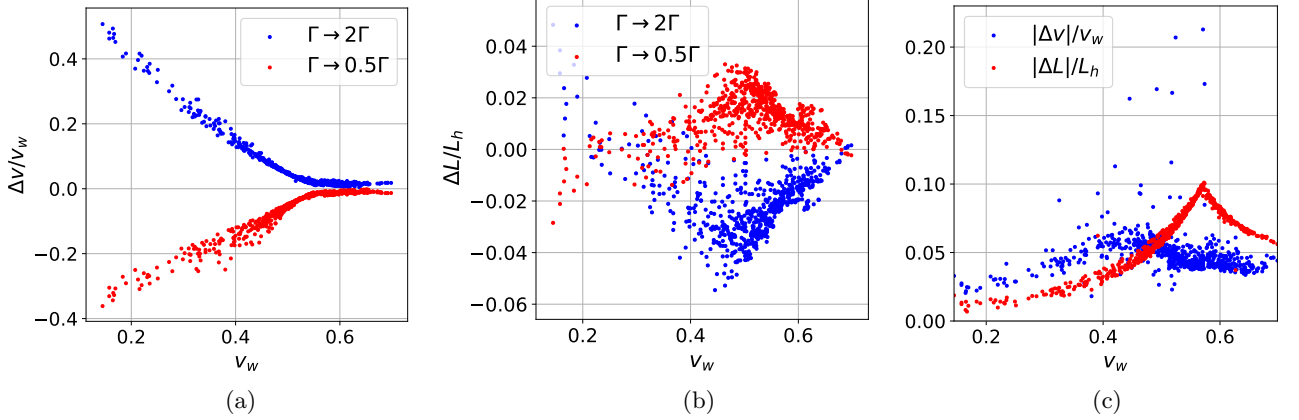


FIG. 10. (a) and (b): Relative changes $\Delta v/v_w$ and $\Delta L/L_h$ in the wall velocities and widths obtained by substituting $\Gamma \rightarrow 2\Gamma$ or $\Gamma/2$ respectively. (c): Absolute error on v_w and L_h due to the discrepancy between the temperatures computed with the Boltzmann equation and the conservation of the energy-momentum tensor (see Eq. (49)).

by $\frac{d}{dT}(\partial V_{\text{eff}}/\partial h)$, so that

$$\Delta_T M_i \approx \int dz \frac{d}{dT} \left(\frac{\partial V_{\text{eff}}}{\partial h} \right) F_i(z) \Delta T(z), \quad (47)$$

where $F_1 = h'$ and $F_2 = h'(2h - h_0)$. We can simplify this integral with the approximation $\Delta T(z) \approx (T_- - T_+)[1 + \tanh(z/L_h)]/2$. Furthermore, we approximate $\frac{d}{dT}(\partial V_{\text{eff}}/\partial h)$ as being constant and half of its maximal value, occurring near $z = 0$. Then

$$\Delta_T M_i \approx \frac{1}{2}(T_- - T_+) C_i \left. \frac{d}{dT} \left(\frac{\partial V_{\text{eff}}}{\partial h} \right) \right|_{z=0}, \quad (48)$$

where $C_1 = \int dz F_1(z)[1 + \tanh(z/L_h)]/2 = h_0/2$ and $C_2 = h_0^2/6$. Substituting this expression in Eq. (46), we finally obtain that the errors on v_w and L_h are given by

$$\begin{aligned} |\Delta v| &\approx \left\{ \left| \frac{1}{4}(T_- - T_+) h_0 \frac{d}{dT} \left(\frac{\partial V_{\text{eff}}}{\partial h} \right) \right|_{z=0} + |\Delta_h M_1| \right\} \left| \frac{\partial M_1}{\partial v_w} \right|^{-1}, \\ |\Delta L| &\approx \left\{ \left| \frac{1}{12}(T_- - T_+) h_0^2 \frac{d}{dT} \left(\frac{\partial V_{\text{eff}}}{\partial h} \right) \right|_{z=0} + |\Delta_h M_2| \right\} \left| \frac{\partial M_2}{\partial L_h} \right|^{-1}. \end{aligned} \quad (49)$$

The relative errors are presented in Fig. 10 (c) for the scan with $\lambda_s = 1$ and $\Lambda = 540$ GeV. The error on v_w is below 7% for 97% of the models, and exhibits no strong correlation with v_w . This happens because $\Delta T = T_- - T_+$ and dM_1/dv_w are roughly proportional (see Fig. 6), and therefore cancel each others' contributions. The relative error on L_h is small at low velocity (or large L_h), but becomes more significant near the speed of sound, however without ever exceeding 10%.

E. Comparison of the GW signal with previous studies

We end this section with a brief comparison with recent studies of the GW produced during a first-order electroweak phase transition. With the prospect of the upcoming LISA experiment, numerous forecasts of the GW spectrum have been made for various extensions of the Standard Model [40, 42, 103–105]. Most of these find regions of model parameter space that would produce detectable GWs. Here we focus on studies of the singlet scalar extensions [37, 38, 41, 106, 107].

Our results agree qualitatively with the conclusions of previous work, in the prediction of GWs detectable by LISA, DECIGO and BBO. However there are distinctions stemming from differences in methodology. To compute

the GW contribution from the sound waves, previous authors used the numerical fit presented in Ref. [6], while we used the updated formula of Ref. [7, 83]. This leads to a smaller peak frequency, decreasing the number of detectable models.

A more significant difference arises from our determination of the wall velocity, which was treated as a free parameter in previous work, whereas we have computed it from the microphysics. The GW spectrum and hence signal-to-noise ratio and ultimately the detectability are strongly dependent on the wall speed. For example, Ref. [106] assumed $v_w = 0.95$ for all models, which considerably enhanced GW production and led to more optimistic predictions. Moreover, using a fixed value for v_w hides the discontinuous transition between the deflagration and detonation solutions shown in Fig. 8 and in Table II. One could therefore incorrectly conclude that some models both yield successful EWBG and GWs detectable by LISA. Our more detailed analysis indicates that LISA will only probe detonation solutions with $v_w \approx 1$, which are incompatible with EWBG.

VII. CONCLUSION

In this work we have taken a first step toward making complete predictions for baryogenesis and gravity waves from a first order electroweak phase transition, starting from a renormalizable Lagrangian that gives rise to the effective operator needed for CP-violation. This is in contrast to previous studies in which quantities like the bubble wall velocity or thickness were treated as free parameters, instead of being derived from the microphysical input parameters as we have done here. This is a necessary step for properly assessing the chances of having successful EWBG and potentially observable GWs, since the two observables are correlated in a nontrivial way, when they are both computed from first principles.

We have incorporated improved fluid equations, both for the CP-even perturbations that determine the friction acting on the bubble wall [56], and for the CP-odd ones that are necessary for baryogenesis [55], that can properly account for wall speeds close to the sound barrier. Earlier versions of these equations were singular at the sound speed, making reliable predictions impossible for fast-moving walls. Contrary to previous lore, we find that EWBG can be more efficient for faster walls, due in part to the tendency for fast walls to be thinner.

The Z_2 -symmetric singlet model with vector-like top partners, analyzed in this work, was chosen for its simplicity, but the methods we used can be applied to other particle physics models that could enhance the EWPT. For example, singlets with no Z_2 symmetry have additional parameters, and would thus be likely to have more freedom to simultaneously yield large GW production and sufficient baryogenesis. It would be interesting to identify other UV-completed models with these properties. A limitation we identified with the Z_2 -symmetric model is that for the large values of the η_2 coupling that are desired for EWBG, the singlet self-coupling is rapidly driven toward zero by renormalization group running, above the top partner threshold.

Acknowledgments. We thank T. Flacke, M. Lewicki and G. Servant for helpful correspondence. The work of JC and BL was supported by the Natural Sciences and Engineering Research Council (Canada). The work of KK was supported by the Academy of Finland grant 31831.

Appendix A: Effective Potential

We describe here the full effective potential used to describe the phase transition in the Z_2 -symmetric singlet model. It takes the general form

$$V_{\text{eff}}(h, s, T) = V_{\text{tree}}(h, s) + V_{\text{CW}}(h, s, T) + V_T(h, s, T) + \delta V(h, s). \quad (\text{A1})$$

V_{tree} is the scalar degrees of freedom's tree-level potential obtained in the unitary gauge by setting in Eq. (1) $H \rightarrow h/\sqrt{2}$ and by omitting the V_{BG} term:

$$V_{\text{tree}}(h, s) = \frac{\mu_h^2}{2} h^2 + \frac{\lambda_h}{4} h^4 + \frac{\lambda_{hs}}{4} h^2 s^2 + \frac{\mu_s^2}{2} s^2 + \frac{\lambda_s}{4} s^4. \quad (\text{A2})$$

V_{CW} is the Coleman-Weinberg potential in the $\overline{\text{MS}}$ renormalization scheme that incorporates the vacuum one-loop corrections and V_T is the thermal potential:

$$V_{\text{CW}}(h, s, T) = \frac{1}{64\pi^2} \sum_{i=W, Z, \gamma_L, 1, 2, \chi, t} n_i \tilde{\mathcal{M}}_i^4(h, s, T) \left[\log \frac{\tilde{\mathcal{M}}_i^2(h, s, T)}{\mu^2} - C_i \right],$$

$$V_T(h, s, T) = \sum_{i=W, Z, \gamma_L, 1, 2, \chi, t} \frac{n_i T^4}{2\pi^2} \int_0^\infty dy y^2 \log \left[1 \pm e^{-\sqrt{y^2 + \tilde{\mathcal{M}}_i^2(h, s, T)/T^2}} \right] - \frac{\tilde{g}\pi^2 T^4}{90}, \quad (\text{A3})$$

where the sums go over all the massive particles, including the thermal mass. Here, we include the contribution from the W and Z gauge bosons, the photon's longitudinal polarization γ_L , the Goldstone bosons χ , the top quark and the eigenvalues of the mass matrix of the Higgs boson and singlet scalar m_1 and m_2 . We impose the renormalization energy scale as $\mu = v$, where $v = 246$ GeV is the Higgs vacuum expectation value. The \pm in the thermal integral is $+$ for fermion and $-$ for bosons and $\tilde{g} = \sum_B N_B + \frac{7}{8} \sum_F N_F = 85.25$ with the sums running over all the lighter degrees of freedom not included in the first term of V_T . The C_i 's are constants given by

$$C_{1,2,\chi,t} = 3/2 \quad \text{and} \quad C_{W,Z,\gamma_L} = 5/6, \quad (\text{A4})$$

and the n_i 's are the particle's number of degrees of freedom:

$$n_{W_T} = 4, n_{W_L} = n_{Z_T} = 2, n_{Z_L} = n_{\gamma_L} = 1, n_{1,2} = 1, n_\chi = 3, n_t = -12. \quad (\text{A5})$$

We adopt the method developed by Parwani [59] to resum the Matsubara zero-modes for the bosonic degrees of freedom. It consists of replacing the bosons' vacuum mass $m_i^2(h, s)$ by the thermal-corrected one $\tilde{\mathcal{M}}_i^2(h, s, T) = m_i^2(h, s) + \Pi_i(T)$, with the self-energy given by

$$\Pi_s(T) = \left(\frac{1}{4} \lambda_s + \frac{1}{6} \lambda_{sh} \right) T^2,$$

$$\Pi_h(T) = \Pi_\chi(T) = \left[\frac{1}{16} (3g_1^2 + g_2^2) + \frac{1}{2} \lambda_h + \frac{1}{4} y_t^2 + \frac{1}{24} \lambda_{hs} \right] T^2, \quad (\text{A6})$$

$$\Pi_{W_L}(T) = \frac{11}{6} g_1^2 T^2,$$

$$\Pi_{W_T}(T) = \Pi_{Z_T}(T) = \Pi_{\gamma_T}(T) = 0.$$

The thermal masses for the longitudinal mode of the photon and Z boson are

$$\tilde{\mathcal{M}}_{Z_L}^2(s, h, T) = \frac{1}{2} \left[m_Z^2(s, h) + \frac{11}{6} \frac{g_1^2}{\cos^2 \theta_w} T^2 + \Delta(s, h, T) \right] \quad \text{and} \quad (\text{A7})$$

$$\tilde{\mathcal{M}}_{\gamma_L}^2(s, h, T) = \frac{1}{2} \left[m_Z^2(s, h) + \frac{11}{6} \frac{g_1^2}{\cos^2 \theta_w} T^2 - \Delta(s, h, T) \right],$$

with

$$\Delta(s, h, T) = \left[m_Z^4(s, h) + \frac{11}{3} \frac{g_1^2 \cos^2 2\theta_w}{\cos^2 \theta_w} \left(m_Z^2(s, h) + \frac{11}{12} \frac{g_1^2}{\cos^2 \theta_w} T^2 \right) T^2 \right]^{1/2}. \quad (\text{A8})$$

At low temperature ($m_i^2/T^2 \gg 1$), one would expect all the thermal effects to be Boltzmann suppressed, since the species i becomes essentially absent from the plasma. This is manifestly the case for V_T , since the thermal integrals decay exponentially in the limit $\tilde{\mathcal{M}}_i^2/T^2 \approx m_i^2/T^2 \gg 1$. However, in the same limit, V_{CW} would depend quadratically on T if we used the thermal masses defined above. This would spoil the potential's low- T behaviour. Therefore, we define a regulated thermal mass¹² $\tilde{\mathcal{M}}_i^2 = m_i^2 + R(m_i^2/T^2)\Pi_i$, that should only be used in V_{CW} . $R(x)$ is a regulator chosen to recover the right behaviour in the low and high- T limit. In order to do so, it should

¹² For the photon and Z boson's longitudinal mode, we define $\Pi_i = \tilde{\mathcal{M}}_i^2 - m_i^2$, which should reproduce the desired behaviour.

be a smooth function satisfying $R(x = 0) = 1$ and $R(x) \sim e^{-\sqrt{|x|}}$ when $|x| \gg 1$. We choose here the integrated Boltzmann number density function given by

$$R(x) = \frac{1}{2}[x]K_2\left(\sqrt{|x|}\right), \quad (\text{A9})$$

where K_2 is the modified Bessel function of the second kind and $[x] = x \tanh(x)$ is a smoothed absolute value.

The last term of Eq. (A1) contains the following counterterms:

$$\delta V(h, s) = Ah^2 + Bh^4 + Cs^2 + D, \quad (\text{A10})$$

which are fixed by requiring the renormalization conditions

$$\begin{aligned} 0 &= \frac{\partial V_{\text{eff}}}{\partial h} \Big|_{h=v, s=0, T=0} \\ m_h^2 &= \frac{\partial^2 V_{\text{eff}}}{\partial h^2} \Big|_{h=v, s=0, T=0} \\ m_s^2 &= \frac{\partial^2 V_{\text{eff}}}{\partial s^2} \Big|_{h=v, s=0, T=0} \\ 0 &= V_{\text{eff}} \Big|_{h=v, s=0, T=0}. \end{aligned} \quad (\text{A11})$$

Appendix B: Relativistic fluid equation

We here calculate the hydrodynamical properties of the plasma close to the wall using the method described in Ref. [81]. The quantities of interest are the temperatures T_{\pm} and the velocities of the plasma measured in the wall frame v_{\pm} . The subscript + and - indicate that the quantity is measured in front or behind the wall respectively.

By integrating the conservation of the energy-momentum tensor equation across the wall, one can show that the quantities T_{\pm} and v_{\pm} are related by the equations

$$\begin{aligned} v_+ v_- &= \frac{1 - (1 - 3\alpha_+)r}{3 - 3(1 + \alpha_+)r}, \\ \frac{v_+}{v_-} &= \frac{3 + (1 - 3\alpha_+)r}{1 + 3(1 + \alpha_+)r}, \end{aligned} \quad (\text{B1})$$

where α_+ and r are defined as

$$\begin{aligned} \alpha_+ &\equiv \frac{\epsilon_+ - \epsilon_-}{a_+ T_+^4}, \\ r &\equiv \frac{a_+ T_+^4}{a_- T_-^4}, \\ a_{\pm} &\equiv -\frac{3}{4T_{\pm}^3} \frac{\partial V_{\text{eff}}}{\partial T} \Big|_{\pm}, \\ \epsilon_{\pm} &\equiv \left(-\frac{T_{\pm}}{4} \frac{\partial V_{\text{eff}}}{\partial T} + V_{\text{eff}} \right) \Big|_{\pm}. \end{aligned} \quad (\text{B2})$$

These quantities are often approximated by the so-called bag equation of state, which is given in Ref. [81]. This approximation is expected to hold when the masses of the plasma's degrees of freedom are very different from T , which is not necessarily true in the broken phase. Therefore, we keep the full relations (B2) in our calculations.

Subsonic walls always come with a shock wave in front of the phase transition front. The Eqs. B1 can be used to relate T_{\pm} and v_{\pm} at the wall and the shock wave, but we need to understand how the temperature and fluid velocity evolve between these two regions. Assuming a spherical bubble and a thin wall, one can derive from the conservation of the energy-momentum tensor the following differential equations

$$\begin{aligned} 2\frac{v}{\xi} &= \gamma^2(1 - v\xi) \left(\frac{\mu^2}{c_s^2} - 1 \right) \partial_{\xi} v, \\ \partial_{\xi} T &= T\gamma^2\mu\partial_{\xi} v, \end{aligned} \quad (\text{B3})$$

where v is the fluid velocity in the frame of the bubble's center and $\xi = r/t$ is the independent variable, with r the distance from the bubble center t the time since the bubble nucleation. With that choice of coordinates, the wall is positioned at $\xi = v_w$. μ is the Lorentz-transformed fluid velocity

$$\mu(\xi, v) = \frac{\xi - v}{1 - \xi v}, \quad (\text{B4})$$

and c_s is the speed of sound in the plasma

$$c_s^2 = \frac{\partial V_{\text{eff}}/\partial T}{T \partial^2 V_{\text{eff}}/\partial T^2} \approx \frac{1}{3}. \quad (\text{B5})$$

The last approximation is valid for relativistic fluids, which models well the unbroken phase. In the broken phase, the particles get a mass that can be of the same order as the temperature, and it causes the speed of sound to become slightly smaller.

One can find three different types of solutions for the fluid's velocity profile: deflagration walls ($v_w < c_s^-$) have a shock wave propagating in front of the wall, detonation walls ($v_w > \xi_J$) have a rarefaction wave behind it and hybrid walls ($c_s^- < v_w < \xi_J$) have both shock and rarefaction waves. ξ_J is the model-dependent Jouguet velocity, which is defined as the smallest velocity a detonation solution can have. Each type of wall have different boundary conditions that determine the characteristics of the solution. Detonation walls are supersonic solutions where the fluid in front of the wall is unperturbed. Therefore, it satisfies the boundary conditions $v_+ = v_w$ and $T_+ = T_n$. For that type of solution, Eqs. (B1) can be solved directly for v_- and T_- .

Subsonic walls always have a deflagration solution with a shock wave at a position ξ_{sh} that solves the equation $v_{sh}^- \xi_{sh} = (c_s^+)^2$, where v_{sh}^- is the fluid's velocity just behind the shock wave measured in the shock wave's frame. It satisfies the boundary conditions $v_- = v_w$ and $T_{sh}^+ = T_n$. Because these boundary conditions are given at two different points, the solution of this system can be somewhat more involved than for the detonation case. Indeed, one has to use a shooting method which consists of choosing an arbitrary value for T_- , solving Eqs. (B1) for T_+ and v_+ , integrating Eqs. (B3) with the initial values $T(v_w) = T_+$ and $v(v_w) = \mu(v_w, v_+)$ until the equation $\mu(\xi, v(\xi))\xi = (c_s^+)^2$ gets satisfied. One can then restart this procedure with a different value of T_- until the Eqs. (B1) are satisfied at the shock wave. Hybrid walls satisfy $v_+ < c_s^- < v_w$ and they have the boundary conditions $v_- = c_s^-$ and $T_{sh}^+ = T_n$, which make them very similar to the deflagration walls.

Appendix C: Gravitational Wave Production

For the convenience of the reader, we here reproduce the formulae from Refs. [7, 81, 83] that determine the GW spectrum from sound waves and turbulence in a first order phase transition. They are given respectively by

$$\Omega_{\text{sw}}(f) = 8.82 \times 10^{-7} K_{\text{sw}}^2 \left(\frac{HR}{c_s} \right) \min \left[1, \frac{HR}{\sqrt{K_{\text{sw}}}} \right] \left(\frac{100}{g_*} \right)^{1/3} S_{\text{sw}}(f), \quad (\text{C1})$$

where $K_{\text{sw}} = \kappa_{\text{sw}} \alpha / (1 + \alpha)$, with κ_{sw} the efficiency coefficient of the sound wave, and $h = 0.678$ is the reduced Hubble constant defined by $H_0 = 100h \text{ km s}^{-1} \text{ Mpc}^{-1}$ [108]. As previously stated, we assume that all the walls have non-runaway solutions and that the contribution from turbulence is negligible; hence we set $\Omega_{\text{sw}} = \Omega_\phi(f) = 0$. The function parametrizing the shape of the GW spectrum is

$$S_{\text{sw}}(f) = \left(\frac{f}{f_{\text{sw}}} \right)^3 \left(\frac{7}{4 + 3(f/f_{\text{sw}})^2} \right)^{\frac{7}{2}}, \quad (\text{C2})$$

and the peak frequency f_{sw} is

$$f_{\text{sw}} = 2.6 \times 10^{-5} \text{ Hz} \left(\frac{1}{HR} \right) \left(\frac{T_n}{100 \text{ GeV}} \right) \left(\frac{g_*}{100} \right)^{\frac{1}{6}}. \quad (\text{C3})$$

Numerical fits for the efficiency coefficient κ_{sw} (the fractions of the available vacuum energy that go into kinetic energy) were presented in [81]. For non-runaway walls, these fits depend on the wall velocity and are given by

$$\kappa_{\text{sw}} = \begin{cases} \frac{c_s^{11/5} \kappa_a \kappa_b}{(c_s^{11/5} - v_w^{11/5}) \kappa_b + v_w c_s^{6/5} \kappa_a}, & v_w \lesssim c_s \\ \kappa_b + (v_w - c_s) \delta \kappa + \frac{(v_w - c_s)^3}{(\xi_J - c_s)^3} [\kappa_c - \kappa_b - (\xi_J - c_s) \delta \kappa], & c_s < v_w < \xi_J \\ \frac{(\xi_J - 1)^3 \xi_J^{5/2} v_w^{-5/2} \kappa_c \kappa_d}{[(\xi_J - 1)^3 - (v_w - 1)^3] \xi_J^{5/2} \kappa_c + (v_w - 1)^3 \kappa_d}, & v_w \gtrsim \xi_J \end{cases} \quad (\text{C4})$$

where $c_s = 1/\sqrt{3}$ is the sound velocity and the different parameters are given by

$$\begin{aligned} \xi_J &= \frac{\sqrt{2\alpha/3 + \alpha^2} + c_s}{1 + \alpha} & \delta \kappa &= -0.9 \log \frac{\sqrt{\alpha}}{1 + \sqrt{\alpha}} \\ \kappa_a &= \frac{6.9 v_w^{6/5} \alpha}{1.36 - 0.037 \sqrt{\alpha} + \alpha} & \kappa_b &= \frac{\alpha^{2/5}}{0.017 + (0.997 + \alpha)^{2/5}} \\ \kappa_c &= \frac{\sqrt{\alpha}}{0.135 + \sqrt{0.98 + \alpha}} & \kappa_d &= \frac{\alpha}{0.73 + 0.083 \sqrt{\alpha} + \alpha} \end{aligned} \quad (\text{C5})$$

We caution that while these fits, when used as input for a signal-to-noise estimate, are useful to get an overall estimate for the Gravitational wave signal in a given model, their precise predictions should be interpreted with care. The fit for the sound wave production is rather reliable for relatively weak transitions $\alpha < 0.1$, which is the range where most of our models luckily fall into. For stronger transitions the fit can overestimate the GW-signal by as much as a factor of thousand (strong deflagrations) [109]. In addition to the strength of the transition, fit parameters have also shown be sensitive on the shape of the effective potential [110].

REFERENCES

- [1] A. I. Bochkarev, S. V. Kuzmin, and M. E. Shaposhnikov, “Electroweak baryogenesis and the Higgs boson mass problem,” *Phys. Lett.* **B244** (1990) 275–278.
- [2] A. G. Cohen, D. B. Kaplan, and A. E. Nelson, “Weak scale baryogenesis,” *Phys. Lett.* **B245** (1990) 561–564.
- [3] A. G. Cohen, D. B. Kaplan, and A. E. Nelson, “Baryogenesis at the weak phase transition,” *Nucl. Phys.* **B349** (1991) 727–742.
- [4] N. Turok and J. Zadrozny, “Electroweak baryogenesis in the two doublet model,” *Nucl. Phys.* **B358** (1991) 471–493.
- [5] A. J. Long, A. Tesi, and L.-T. Wang, “Baryogenesis at a Lepton-Number-Breaking Phase Transition,” *JHEP* **10** (2017) 095, [arXiv:1703.04902 \[hep-ph\]](https://arxiv.org/abs/1703.04902).
- [6] C. Caprini *et al.*, “Science with the space-based interferometer eLISA. II: Gravitational waves from cosmological phase transitions,” *JCAP* **04** (2016) 001, [arXiv:1512.06239 \[astro-ph.CO\]](https://arxiv.org/abs/1512.06239).
- [7] C. Caprini *et al.*, “Detecting gravitational waves from cosmological phase transitions with LISA: an update,” *JCAP* **03** (2020) 024, [arXiv:1910.13125 \[astro-ph.CO\]](https://arxiv.org/abs/1910.13125).
- [8] J. Crowder and N. J. Cornish, “Beyond LISA: Exploring future gravitational wave missions,” *Phys. Rev. D* **72** (2005) 083005, [arXiv:gr-qc/0506015](https://arxiv.org/abs/gr-qc/0506015).
- [9] N. Seto, S. Kawamura, and T. Nakamura, “Possibility of direct measurement of the acceleration of the universe using 0.1-Hz band laser interferometer gravitational wave antenna in space,” *Phys. Rev. Lett.* **87** (2001) 221103, [arXiv:astro-ph/0108011](https://arxiv.org/abs/astro-ph/0108011).
- [10] S. Sato *et al.*, “The status of DECIGO,” *J. Phys. Conf. Ser.* **840** no. 1, (2017) 012010.
- [11] **AEDGE** Collaboration, Y. A. El-Neaj *et al.*, “AEDGE: Atomic Experiment for Dark Matter and Gravity Exploration in Space,” *EPJ Quant. Technol.* **7** (2020) 6, [arXiv:1908.00802 \[gr-qc\]](https://arxiv.org/abs/1908.00802).
- [12] K. Kajantie, M. Laine, K. Rummukainen, and M. E. Shaposhnikov, “A Nonperturbative analysis of the finite T phase transition in $SU(2) \times U(1)$ electroweak theory,” *Nucl. Phys.* **B493** (1997) 413–438, [arXiv:hep-lat/9612006 \[hep-lat\]](https://arxiv.org/abs/hep-lat/9612006).
- [13] K. Kajantie, M. Laine, K. Rummukainen, and M. E. Shaposhnikov, “Is there a hot electroweak phase transition at $m(H)$ larger or equal to $m(W) ?$,” *Phys. Rev. Lett.* **77** (1996) 2887–2890, [arXiv:hep-ph/9605288 \[hep-ph\]](https://arxiv.org/abs/hep-ph/9605288).
- [14] G. W. Anderson and L. J. Hall, “The Electroweak phase transition and baryogenesis,” *Phys. Rev. D* **45** (1992) 2685–2698.
- [15] J. McDonald, “Electroweak baryogenesis and dark matter via a gauge singlet scalar,” *Phys. Lett. B* **323** (1994) 339–346.
- [16] J. Choi and R. R. Volkas, “Real Higgs singlet and the electroweak phase transition in the Standard Model,” *Phys. Lett. B* **317** (1993) 385–391, [arXiv:hep-ph/9308234](https://arxiv.org/abs/hep-ph/9308234).

- [17] J. R. Espinosa and M. Quiros, “Novel Effects in Electroweak Breaking from a Hidden Sector,” *Phys. Rev. D* **76** (2007) 076004, [arXiv:hep-ph/0701145](https://arxiv.org/abs/hep-ph/0701145).
- [18] S. Profumo, M. J. Ramsey-Musolf, and G. Shaughnessy, “Singlet Higgs phenomenology and the electroweak phase transition,” *JHEP* **08** (2007) 010, [arXiv:0705.2425 \[hep-ph\]](https://arxiv.org/abs/0705.2425).
- [19] J. R. Espinosa, T. Konstandin, and F. Riva, “Strong Electroweak Phase Transitions in the Standard Model with a Singlet,” *Nucl. Phys. B* **854** (2012) 592–630, [arXiv:1107.5441 \[hep-ph\]](https://arxiv.org/abs/1107.5441).
- [20] G. Kurup and M. Perelstein, “Dynamics of Electroweak Phase Transition In Singlet-Scalar Extension of the Standard Model,” *Phys. Rev. D* **96** no. 1, (2017) 015036, [arXiv:1704.03381 \[hep-ph\]](https://arxiv.org/abs/1704.03381).
- [21] S. W. Ham, Y. S. Jeong, and S. K. Oh, “Electroweak phase transition in an extension of the standard model with a real Higgs singlet,” *J. Phys. G* **31** no. 8, (2005) 857–871, [arXiv:hep-ph/0411352](https://arxiv.org/abs/hep-ph/0411352).
- [22] A. Noble and M. Perelstein, “Higgs self-coupling as a probe of electroweak phase transition,” *Phys. Rev. D* **78** (2008) 063518, [arXiv:0711.3018 \[hep-ph\]](https://arxiv.org/abs/0711.3018).
- [23] D. Curtin, P. Meade, and C.-T. Yu, “Testing Electroweak Baryogenesis with Future Colliders,” *JHEP* **11** (2014) 127, [arXiv:1409.0005 \[hep-ph\]](https://arxiv.org/abs/1409.0005).
- [24] S. Profumo, M. J. Ramsey-Musolf, C. L. Wainwright, and P. Winslow, “Singlet-catalyzed electroweak phase transitions and precision Higgs boson studies,” *Phys. Rev. D* **91** no. 3, (2015) 035018, [arXiv:1407.5342 \[hep-ph\]](https://arxiv.org/abs/1407.5342).
- [25] A. V. Kotwal, M. J. Ramsey-Musolf, J. M. No, and P. Winslow, “Singlet-catalyzed electroweak phase transitions in the 100 TeV frontier,” *Phys. Rev. D* **94** no. 3, (2016) 035022, [arXiv:1605.06123 \[hep-ph\]](https://arxiv.org/abs/1605.06123).
- [26] P. Huang, A. J. Long, and L.-T. Wang, “Probing the Electroweak Phase Transition with Higgs Factories and Gravitational Waves,” *Phys. Rev. D* **94** no. 7, (2016) 075008, [arXiv:1608.06619 \[hep-ph\]](https://arxiv.org/abs/1608.06619).
- [27] K. Hashino, R. Jinno, M. Kakizaki, S. Kanemura, T. Takahashi, and M. Takimoto, “Selecting models of first-order phase transitions using the synergy between collider and gravitational-wave experiments,” *Phys. Rev. D* **99** no. 7, (2019) 075011, [arXiv:1809.04994 \[hep-ph\]](https://arxiv.org/abs/1809.04994).
- [28] M. J. Ramsey-Musolf, “The electroweak phase transition: a collider target,” *JHEP* **09** (2020) 179, [arXiv:1912.07189 \[hep-ph\]](https://arxiv.org/abs/1912.07189).
- [29] K.-P. Xie, “Lepton-mediated electroweak baryogenesis, gravitational waves and the 4τ final state at the collider,” [arXiv:2011.04821 \[hep-ph\]](https://arxiv.org/abs/2011.04821).
- [30] S. Das, P. J. Fox, A. Kumar, and N. Weiner, “The Dark Side of the Electroweak Phase Transition,” *JHEP* **11** (2010) 108, [arXiv:0910.1262 \[hep-ph\]](https://arxiv.org/abs/0910.1262).
- [31] A. Ashoorioon and T. Konstandin, “Strong electroweak phase transitions without collider traces,” *JHEP* **07** (2009) 086, [arXiv:0904.0353 \[hep-ph\]](https://arxiv.org/abs/0904.0353).
- [32] M. Kakizaki, S. Kanemura, and T. Matsui, “Gravitational waves as a probe of extended scalar sectors with the first order electroweak phase transition,” *Phys. Rev. D* **92** no. 11, (2015) 115007, [arXiv:1509.08394 \[hep-ph\]](https://arxiv.org/abs/1509.08394).
- [33] K. Hashino, M. Kakizaki, S. Kanemura, and T. Matsui, “Synergy between measurements of gravitational waves and the triple-Higgs coupling in probing the first-order electroweak phase transition,” *Phys. Rev. D* **94** no. 1, (2016) 015005, [arXiv:1604.02069 \[hep-ph\]](https://arxiv.org/abs/1604.02069).
- [34] M. Chala, G. Nardini, and I. Sobolev, “Unified explanation for dark matter and electroweak baryogenesis with direct detection and gravitational wave signatures,” *Phys. Rev. D* **94** no. 5, (2016) 055006, [arXiv:1605.08663 \[hep-ph\]](https://arxiv.org/abs/1605.08663).
- [35] T. Tenkanen, K. Tuominen, and V. Vaskonen, “A Strong Electroweak Phase Transition from the Inflaton Field,” *JCAP* **09** (2016) 037, [arXiv:1606.06063 \[hep-ph\]](https://arxiv.org/abs/1606.06063).
- [36] K. Hashino, M. Kakizaki, S. Kanemura, P. Ko, and T. Matsui, “Gravitational waves and Higgs boson couplings for exploring first order phase transition in the model with a singlet scalar field,” *Phys. Lett. B* **766** (2017) 49–54, [arXiv:1609.00297 \[hep-ph\]](https://arxiv.org/abs/1609.00297).
- [37] V. Vaskonen, “Electroweak baryogenesis and gravitational waves from a real scalar singlet,” *Phys. Rev. D* **95** no. 12, (2017) 123515, [arXiv:1611.02073 \[hep-ph\]](https://arxiv.org/abs/1611.02073).
- [38] A. Beniwal, M. Lewicki, J. D. Wells, M. White, and A. G. Williams, “Gravitational wave, collider and dark matter signals from a scalar singlet electroweak baryogenesis,” *JHEP* **08** (2017) 108, [arXiv:1702.06124 \[hep-ph\]](https://arxiv.org/abs/1702.06124).
- [39] A. Ahriche, K. Hashino, S. Kanemura, and S. Nasri, “Gravitational Waves from Phase Transitions in Models with Charged Singlets,” *Phys. Lett. B* **789** (2019) 119–126, [arXiv:1809.09883 \[hep-ph\]](https://arxiv.org/abs/1809.09883).
- [40] A. Beniwal, M. Lewicki, M. White, and A. G. Williams, “Gravitational waves and electroweak baryogenesis in a global study of the extended scalar singlet model,” *JHEP* **02** (2019) 183, [arXiv:1810.02380 \[hep-ph\]](https://arxiv.org/abs/1810.02380).
- [41] M. Carena, Z. Liu, and Y. Wang, “Electroweak phase transition with spontaneous Z_2 -breaking,” *JHEP* **08** (2020) 107, [arXiv:1911.10206 \[hep-ph\]](https://arxiv.org/abs/1911.10206).
- [42] J. Ellis, M. Lewicki, and V. Vaskonen, “Updated predictions for gravitational waves produced in a strongly supercooled phase transition,” [arXiv:2007.15586 \[astro-ph.CO\]](https://arxiv.org/abs/2007.15586).
- [43] G. D. Moore and T. Prokopec, “How fast can the wall move? A Study of the electroweak phase transition dynamics,” *Phys. Rev. D* **52** (1995) 7182–7204, [arXiv:hep-ph/9506475](https://arxiv.org/abs/hep-ph/9506475).
- [44] G. D. Moore and T. Prokopec, “Bubble wall velocity in a first order electroweak phase transition,” *Phys. Rev. Lett.* **75** (1995) 777–780, [arXiv:hep-ph/9503296](https://arxiv.org/abs/hep-ph/9503296).
- [45] P. John and M. G. Schmidt, “Do stops slow down electroweak bubble walls?,” *Nucl. Phys. B* **598** (2001) 291–305, [arXiv:hep-ph/0002050](https://arxiv.org/abs/hep-ph/0002050). [Erratum: Nucl.Phys.B 648, 449–452 (2003)].
- [46] D. Bodeker and G. D. Moore, “Can electroweak bubble walls run away?,” *JCAP* **05** (2009) 009, [arXiv:0903.4099 \[hep-ph\]](https://arxiv.org/abs/0903.4099).
- [47] J. Kozaczuk, “Bubble Expansion and the Viability of Singlet-Driven Electroweak Baryogenesis,” *JHEP* **10** (2015) 135, [arXiv:1506.04741 \[hep-ph\]](https://arxiv.org/abs/1506.04741).

[48] T. Konstandin and J. M. No, “Hydrodynamic obstruction to bubble expansion,” *JCAP* **02** (2011) 008, [arXiv:1011.3735 \[hep-ph\]](https://arxiv.org/abs/1011.3735).

[49] T. Konstandin, G. Nardini, and I. Rues, “From Boltzmann equations to steady wall velocities,” *JCAP* **09** (2014) 028, [arXiv:1407.3132 \[hep-ph\]](https://arxiv.org/abs/1407.3132).

[50] D. Bodeker and G. D. Moore, “Electroweak Bubble Wall Speed Limit,” *JCAP* **05** (2017) 025, [arXiv:1703.08215 \[hep-ph\]](https://arxiv.org/abs/1703.08215).

[51] S. Höche, J. Kozaczuk, A. J. Long, J. Turner, and Y. Wang, “Towards an all-orders calculation of the electroweak bubble wall velocity,” [arXiv:2007.10343 \[hep-ph\]](https://arxiv.org/abs/2007.10343).

[52] M. Barroso Mancha, T. Prokopec, and B. Swiezewska, “Field-theoretic derivation of bubble-wall force,” [arXiv:2005.10875 \[hep-th\]](https://arxiv.org/abs/2005.10875).

[53] S. Balaji, M. Spannowsky, and C. Tamarit, “Cosmological bubble friction in local equilibrium,” [arXiv:2010.08013 \[hep-ph\]](https://arxiv.org/abs/2010.08013).

[54] A. Friedlander, I. Banta, J. M. Cline, and D. Tucker-Smith, “Wall speed and shape in singlet-assisted strong electroweak phase transitions,” [arXiv:2009.14295 \[hep-ph\]](https://arxiv.org/abs/2009.14295).

[55] J. M. Cline and K. Kainulainen, “Electroweak baryogenesis at high bubble wall velocities,” *Phys. Rev. D* **101** no. 6, (2020) 063525, [arXiv:2001.00568 \[hep-ph\]](https://arxiv.org/abs/2001.00568).

[56] B. Laurent and J. M. Cline, “Fluid equations for fast-moving electroweak bubble walls,” *Phys. Rev. D* **102** no. 6, (2020) 063516, [arXiv:2007.10935 \[hep-ph\]](https://arxiv.org/abs/2007.10935).

[57] W. Waltenberger, A. Lessa, and S. Kraml, “Artificial Proto-Modelling: Building Precursors of a Next Standard Model from Simplified Model Results,” [arXiv:2012.12246 \[hep-ph\]](https://arxiv.org/abs/2012.12246).

[58] J. M. Cline and K. Kainulainen, “Electroweak baryogenesis and dark matter from a singlet Higgs,” *JCAP* **01** (2013) 012, [arXiv:1210.4196 \[hep-ph\]](https://arxiv.org/abs/1210.4196).

[59] R. R. Parwani, “Resummation in a hot scalar field theory,” *Phys. Rev. D* **45** (1992) 4695, [arXiv:hep-ph/9204216](https://arxiv.org/abs/hep-ph/9204216). [Erratum: *Phys. Rev. D* 48, 5965 (1993)].

[60] CMS Collaboration, A. M. Sirunyan *et al.*, “Combined measurements of Higgs boson couplings in proton–proton collisions at $\sqrt{s} = 13$ TeV,” *Eur. Phys. J.* **C79** no. 5, (2019) 421, [arXiv:1809.10733 \[hep-ex\]](https://arxiv.org/abs/1809.10733).

[61] ATLAS Collaboration, G. Aad *et al.*, “Combined measurements of Higgs boson production and decay using up to 80 fb^{-1} of proton-proton collision data at $\sqrt{s} = 13$ TeV collected with the ATLAS experiment,” *Phys. Rev.* **D101** no. 1, (2020) 012002, [arXiv:1909.02845 \[hep-ex\]](https://arxiv.org/abs/1909.02845).

[62] ATLAS Collaboration, M. Aaboud *et al.*, “Combination of the searches for pair-produced vector-like partners of the third-generation quarks at $\sqrt{s} = 13$ TeV with the ATLAS detector,” *Phys. Rev. Lett.* **121** no. 21, (2018) 211801, [arXiv:1808.02343 \[hep-ex\]](https://arxiv.org/abs/1808.02343).

[63] CMS Collaboration, A. M. Sirunyan *et al.*, “Search for vector-like T and B quark pairs in final states with leptons at $\sqrt{s} = 13$ TeV,” *JHEP* **08** (2018) 177, [arXiv:1805.04758 \[hep-ex\]](https://arxiv.org/abs/1805.04758).

[64] G. Brooijmans *et al.*, “Les Houches 2019 Physics at TeV Colliders: New Physics Working Group Report,” in *11th Les Houches Workshop on Physics at TeV Colliders: PhysTeV Les Houches*. 2019. [arXiv:2002.12220 \[hep-ph\]](https://arxiv.org/abs/2002.12220).

[65] G. Cacciapaglia, T. Flacke, M. Park, and M. Zhang, “Exotic decays of top partners: mind the search gap,” *Phys. Lett.* **B798** (2019) 135015, [arXiv:1908.07524 \[hep-ph\]](https://arxiv.org/abs/1908.07524).

[66] S. Dawson and E. Furlan, “A Higgs Conundrum with Vector Fermions,” *Phys. Rev. D* **86** (2012) 015021, [arXiv:1205.4733 \[hep-ph\]](https://arxiv.org/abs/1205.4733).

[67] Particle Data Group Collaboration, M. Tanabashi *et al.*, “Review of Particle Physics,” *Phys. Rev.* **D98** no. 3, (2018) 030001.

[68] N. Craig, P. Draper, C. Kilic, and S. Thomas, “Shedding Light on Diphoton Resonances,” *Phys. Rev.* **D93** no. 11, (2016) 115023, [arXiv:1512.07733 \[hep-ph\]](https://arxiv.org/abs/1512.07733).

[69] ATLAS Collaboration, “Search for resonances decaying to photon pairs in 139 fb^{-1} of pp collisions at $\sqrt{s} = 13$ TeV with the ATLAS detector.,,”

[70] ATLAS Collaboration, T. A. collaboration, “Search for resonances in the 65 to 110 GeV diphoton invariant mass range using 80 fb^{-1} of pp collisions collected at $\sqrt{s} = 13$ TeV with the ATLAS detector.,”

[71] CMS Collaboration, A. M. Sirunyan *et al.*, “Search for a standard model-like Higgs boson in the mass range between 70 and 110 GeV in the diphoton final state in proton-proton collisions at $\sqrt{s} = 8$ and 13 TeV,” *Phys. Lett.* **B793** (2019) 320–347, [arXiv:1811.08459 \[hep-ex\]](https://arxiv.org/abs/1811.08459).

[72] ATLAS Collaboration, G. Aad *et al.*, “Search for new phenomena in events with two opposite-charge leptons, jets and missing transverse momentum in pp collisions at $\sqrt{s} = 13$ TeV with the ATLAS detector,” [arXiv:2102.01444 \[hep-ex\]](https://arxiv.org/abs/2102.01444).

[73] CMS Collaboration, A. M. Sirunyan *et al.*, “Search for top squarks and dark matter particles in opposite-charge dilepton final states at $\sqrt{s} = 13$ TeV,” *Phys. Rev. D* **97** no. 3, (2018) 032009, [arXiv:1711.00752 \[hep-ex\]](https://arxiv.org/abs/1711.00752).

[74] K. Enqvist, J. Ignatius, K. Kajantie, and K. Rummukainen, “Nucleation and bubble growth in a first order cosmological electroweak phase transition,” *Phys. Rev. D* **45** (1992) 3415–3428.

[75] A. D. Linde, “Fate of the False Vacuum at Finite Temperature: Theory and Applications,” *Phys. Lett.* **100B** (1981) 37–40.

[76] M. Quiros, “Finite temperature field theory and phase transitions,” in *Proceedings, Summer School in High-energy physics and cosmology: Trieste, Italy, June 29–July 17, 1998*, pp. 187–259. 1999. [arXiv:hep-ph/9901312 \[hep-ph\]](https://arxiv.org/abs/hep-ph/9901312).

[77] C. L. Wainwright, “CosmoTransitions: Computing Cosmological Phase Transition Temperatures and Bubble Profiles with Multiple Fields,” *Comput. Phys. Commun.* **183** (2012) 2006–2013, [arXiv:1109.4189 \[hep-ph\]](https://arxiv.org/abs/1109.4189).

[78] J. M. Cline, K. Kainulainen, and D. Tucker-Smith, “Electroweak baryogenesis from a dark sector,” *Phys. Rev. D* **95**

no. 11, (2017) 115006, [arXiv:1702.08909 \[hep-ph\]](https://arxiv.org/abs/1702.08909).

[79] S. R. Coleman, “The Fate of the False Vacuum. 1. Semiclassical Theory,” *Phys. Rev. D* **15** (1977) 2929–2936. [Erratum: *Phys. Rev. D* **16**, 1248 (1977)].

[80] M. Kamionkowski, A. Kosowsky, and M. S. Turner, “Gravitational radiation from first order phase transitions,” *Phys. Rev. D* **49** (1994) 2837–2851, [arXiv:astro-ph/9310044](https://arxiv.org/abs/astro-ph/9310044).

[81] J. R. Espinosa, T. Konstandin, J. M. No, and G. Servant, “Energy Budget of Cosmological First-order Phase Transitions,” *JCAP* **06** (2010) 028, [arXiv:1004.4187 \[hep-ph\]](https://arxiv.org/abs/1004.4187).

[82] S. J. Huber and M. Sopena, “An efficient approach to electroweak bubble velocities,” [arXiv:1302.1044 \[hep-ph\]](https://arxiv.org/abs/1302.1044).

[83] M. Hindmarsh, S. J. Huber, K. Rummukainen, and D. J. Weir, “Shape of the acoustic gravitational wave power spectrum from a first order phase transition,” *Phys. Rev. D* **96** no. 10, (2017) 103520, [arXiv:1704.05871 \[astro-ph.CO\]](https://arxiv.org/abs/1704.05871). [Erratum: *Phys. Rev. D* **101**, 089902 (2020)].

[84] A. Roper Pol, S. Mandal, A. Brandenburg, T. Kahniashvili, and A. Kosowsky, “Numerical simulations of gravitational waves from early-universe turbulence,” *Phys. Rev. D* **102** no. 8, (2020) 083512, [arXiv:1903.08585 \[astro-ph.CO\]](https://arxiv.org/abs/1903.08585).

[85] **LISA** Collaboration, P. Amaro-Seoane *et al.*, “Laser Interferometer Space Antenna,” [arXiv:1702.00786 \[astro-ph.IM\]](https://arxiv.org/abs/1702.00786).

[86] V. Corbin and N. J. Cornish, “Detecting the cosmic gravitational wave background with the big bang observer,” *Class. Quant. Grav.* **23** (2006) 2435–2446, [arXiv:gr-qc/0512039](https://arxiv.org/abs/gr-qc/0512039).

[87] E. Thrane and J. D. Romano, “Sensitivity curves for searches for gravitational-wave backgrounds,” *Phys. Rev. D* **88** no. 12, (2013) 124032, [arXiv:1310.5300 \[astro-ph.IM\]](https://arxiv.org/abs/1310.5300).

[88] M. Breitbach, J. Kopp, E. Madge, T. Opferkuch, and P. Schwaller, “Dark, Cold, and Noisy: Constraining Secluded Hidden Sectors with Gravitational Waves,” *JCAP* **07** (2019) 007, [arXiv:1811.11175 \[hep-ph\]](https://arxiv.org/abs/1811.11175).

[89] E. Thrane and J. D. Romano, “Sensitivity curves for searches for gravitational-wave backgrounds,” *Phys. Rev. D* **88** no. 12, (2013) 124032, [arXiv:1310.5300 \[astro-ph.IM\]](https://arxiv.org/abs/1310.5300).

[90] G. D. Moore, “Measuring the broken phase sphaleron rate nonperturbatively,” *Phys. Rev. D* **59** (1999) 014503, [arXiv:hep-ph/9805264](https://arxiv.org/abs/hep-ph/9805264).

[91] K. Fuyuto and E. Senaha, “Improved sphaleron decoupling condition and the Higgs coupling constants in the real singlet-extended standard model,” *Phys. Rev. D* **90** no. 1, (2014) 015015, [arXiv:1406.0433 \[hep-ph\]](https://arxiv.org/abs/1406.0433).

[92] L. Fromme and S. J. Huber, “Top transport in electroweak baryogenesis,” *JHEP* **03** (2007) 049, [arXiv:hep-ph/0604159 \[hep-ph\]](https://arxiv.org/abs/hep-ph/0604159).

[93] J. M. Cline, K. Kainulainen, and M. Trott, “Electroweak Baryogenesis in Two Higgs Doublet Models and B meson anomalies,” *JHEP* **11** (2011) 089, [arXiv:1107.3559 \[hep-ph\]](https://arxiv.org/abs/1107.3559).

[94] A. Riotto, “Towards a nonequilibrium quantum field theory approach to electroweak baryogenesis,” *Phys. Rev. D* **53** (1996) 5834–5841, [arXiv:hep-ph/9510271 \[hep-ph\]](https://arxiv.org/abs/hep-ph/9510271).

[95] A. Riotto, “Supersymmetric electroweak baryogenesis, nonequilibrium field theory and quantum Boltzmann equations,” *Nucl. Phys. B* **518** (1998) 339–360, [arXiv:hep-ph/9712221 \[hep-ph\]](https://arxiv.org/abs/hep-ph/9712221).

[96] M. Joyce, T. Prokopec, and N. Turok, “Nonlocal electroweak baryogenesis. Part 2: The Classical regime,” *Phys. Rev. D* **53** (1996) 2958–2980, [arXiv:hep-ph/9410282 \[hep-ph\]](https://arxiv.org/abs/hep-ph/9410282).

[97] J. M. Cline, M. Joyce, and K. Kainulainen, “Supersymmetric electroweak baryogenesis,” *JHEP* **07** (2000) 018, [arXiv:hep-ph/0006119 \[hep-ph\]](https://arxiv.org/abs/hep-ph/0006119).

[98] K. Kainulainen, T. Prokopec, M. G. Schmidt, and S. Weinstock, “First principle derivation of semiclassical force for electroweak baryogenesis,” *JHEP* **06** (2001) 031, [arXiv:hep-ph/0105295 \[hep-ph\]](https://arxiv.org/abs/hep-ph/0105295).

[99] K. Kainulainen, T. Prokopec, M. G. Schmidt, and S. Weinstock, “Semiclassical force for electroweak baryogenesis: Three-dimensional derivation,” *Phys. Rev. D* **66** (2002) 043502, [arXiv:hep-ph/0202177 \[hep-ph\]](https://arxiv.org/abs/hep-ph/0202177).

[100] T. Prokopec, M. G. Schmidt, and S. Weinstock, “Transport equations for chiral fermions to order \hbar and electroweak baryogenesis. Part 1,” *Annals Phys.* **314** (2004) 208–265, [arXiv:hep-ph/0312110 \[hep-ph\]](https://arxiv.org/abs/hep-ph/0312110).

[101] T. Prokopec, M. G. Schmidt, and S. Weinstock, “Transport equations for chiral fermions to order \hbar -bar and electroweak baryogenesis. Part II,” *Annals Phys.* **314** (2004) 267–320, [arXiv:hep-ph/0406140 \[hep-ph\]](https://arxiv.org/abs/hep-ph/0406140).

[102] H. Jukkala, K. Kainulainen, and O. Koskivaara, “Quantum transport and the phase space structure of the Wightman functions,” *JHEP* **01** (2020) 012, [arXiv:1910.10979 \[hep-th\]](https://arxiv.org/abs/1910.10979).

[103] T. Prokopec, J. Rezacek, and B. Świeżewska, “Gravitational waves from conformal symmetry breaking,” *JCAP* **02** (2019) 009, [arXiv:1809.11129 \[hep-ph\]](https://arxiv.org/abs/1809.11129).

[104] C. Marzo, L. Marzola, and V. Vaskonen, “Phase transition and vacuum stability in the classically conformal B-L model,” *Eur. Phys. J. C* **79** no. 7, (2019) 601, [arXiv:1811.11169 \[hep-ph\]](https://arxiv.org/abs/1811.11169).

[105] P. S. B. Dev, F. Ferrer, Y. Zhang, and Y. Zhang, “Gravitational Waves from First-Order Phase Transition in a Simple Axion-Like Particle Model,” *JCAP* **11** (2019) 006, [arXiv:1905.00891 \[hep-ph\]](https://arxiv.org/abs/1905.00891).

[106] Z. Kang, P. Ko, and T. Matsui, “Strong first order EWPT \& strong gravitational waves in Z_3 -symmetric singlet scalar extension,” *JHEP* **02** (2018) 115, [arXiv:1706.09721 \[hep-ph\]](https://arxiv.org/abs/1706.09721).

[107] A. Alves, T. Ghosh, H.-K. Guo, K. Sinha, and D. Vagie, “Collider and Gravitational Wave Complementarity in Exploring the Singlet Extension of the Standard Model,” *JHEP* **04** (2019) 052, [arXiv:1812.09333 \[hep-ph\]](https://arxiv.org/abs/1812.09333).

[108] **Planck** Collaboration, N. Aghanim *et al.*, “Planck 2018 results. VI. Cosmological parameters,” *Astron. Astrophys.* **641** (2020) A6, [arXiv:1807.06209 \[astro-ph.CO\]](https://arxiv.org/abs/1807.06209).

[109] D. Cutting, M. Hindmarsh, and D. J. Weir, “Vorticity, kinetic energy, and suppressed gravitational wave production in strong first order phase transitions,” *Phys. Rev. Lett.* **125** no. 2, (2020) 021302, [arXiv:1906.00480 \[hep-ph\]](https://arxiv.org/abs/1906.00480).

[110] D. Cutting, E. G. Escartin, M. Hindmarsh, and D. J. Weir, “Gravitational waves from vacuum first order phase

transitions II: from thin to thick walls,” [arXiv:2005.13537 \[astro-ph.CO\]](https://arxiv.org/abs/2005.13537).

